Seismic *Lg*-wave *Q* tomography in and around Northeast China

Lian-Feng Zhao,[1] Xiao-Bi Xie,[2] Wei-Min Wang,[3] Jin-Hai Zhang,[1] and Zhen-Xing Yao[1]

[1]   We investigate regional variations in the *Lg*-wave quality factor (Q) in Northeast China and its vicinity with a tomographic method. Digital seismic data recorded at 20 broadband stations from 125 regional events are used to extract *Lg*-wave spectra. Tomographic inversions are independently conducted at 58 discrete frequencies distributed log evenly between 0.05 and 10.0 Hz. We simultaneously invert for the *Lg*-wave Q distribution and source spectra at individual frequencies without using any a priori assumption about the frequency dependence of the Q model and source function. The best spatial resolution is approximately $1° \times 1°$ in well-covered areas for frequencies between 0.4 and 2.0 Hz. The *Lg Q* shows significant regional variations and an apparent relationship with regional geology. We use a statistical method to investigate the regional variations of *Lg Q* and their frequency dependence. The average Q_0 (1 Hz *Lg Q*) in the entire investigated region is 414. Sedimentary basins are usually characterized by lower average Q_0 values (from 155 to 391), while volcanic mountain areas have relatively high average Q_0 values (from 630 to 675). *Lg Q* generally increases with increasing frequency. However, the frequency dependence has complex nonlinear features on a double-logarithmic scale, indicating that the commonly adopted power-law relationship may be oversimplified in a broad frequency band. The frequency dependence varies in different geological areas, with larger variations seen at lower frequencies.

Citation: Zhao, L.-F., X.-B. Xie, W.-M. Wang, J.-H. Zhang, and Z.-X. Yao (2010), Seismic *Lg*-wave *Q* tomography in and around Northeast China, *J. Geophys. Res.*, *115*, B08307, doi:10.1029/2009JB007157.

1.   Introduction

[2]   The *Lg* wave is one of the most prominent seismic phases in high-frequency seismograms observed over continental paths at regional to teleseismic distances. It is usually understood to be a sum of higher mode surface waves propagating in the crustal waveguide or multiply reflected *S* waves supercritically bouncing between the free surface and the Moho discontinuity [*Knopoff et al.*, 1973; *Bouchon*, 1982; *Kennett*, 1984; *Xie and Lay*, 1994]. Thus, the *Lg* wave samples the crust waveguide relatively evenly. It is also sensitive to the characteristics of the free surface and the Moho discontinuity and to the crustal thickness. Given these attributes, much attention has been paid to *Lg*-wave data for investigating the properties of the crust.

[3]   The *Lg*-wave quality factor *Q* (Q_{Lg}) describes the attenuation of *Lg* signals and is one of the basic parameters useful for characterizing the Earth's crust. Scattering losses and intrinsic attenuation are both responsible for the ampli-tude decay of *Lg* waves. *Lg*-wave scattering is closely related to the heterogeneities of all scales in the crustal waveguide. Thus, *Lg* waves and *Lg* coda have been used successfully for the past three decades to infer and measure the attenuation and scattering structure of the crust [*Nuttli*, 1973; *Kadinsky-Cade et al.*, 1981; *Xie and Nuttli*, 1988; *McNamara et al.*, 1996; *Mitchell et al.*, 1997; *Rodgers et al.*, 1997; *Cong and Mitchell*, 1998; *Mellors et al.*, 1999; *Philips et al.*, 2000; *Wu et al.*, 2000; *Sandvol et al.*, 2001; *Fan and Lay*, 2002, 2003a, b; *Ottemöller*, 2002; *Ottemöller et al.*, 2002; *Xie et al.*, 2004, 2006; *Phillips et al.*, 2005; *Zor et al.*, 2007; *Mitchell et al.*, 2008; *Phillips and Stead*, 2008]. Q_{Lg} depends on the types of material, thermal status, and degree of heterogeneities in the crust. In general, high Q_{Lg} values correlate well with stable ancient crust, while relatively low Q_{Lg} values correlate well with recently deformed crust and active tectonic environments [e.g., *Fan and Lay*, 2002, 2003a, b; *Xie et al.*, 2004, 2006; *Phillips et al.*, 2005]. Several studies have also suggested that crustal thickness or undulation of the Moho discontinuity can result in significant *Lg*-wave attenuation and that both the oceanic crust and the sedimentary basins can strongly attenuate or even block *Lg* waves by disrupting their underlying mode structures [e.g., *Kennett*, 1986; *Campillo*, 1987; *Campillo et al.*, 1993; *Zhang and Lay*, 1995; *Shapiro et al.*, 1996; *Wu et al.*, 2000].

[4]   Northeast China is a complex convergence zone between several large-scale geological units including the West Pacific tectonic belt, the Siberian plate, the North China

[1]Institute of Geology and Geophysics, Chinese Academy of Sciences, Beijing, China.
[2]Institute of Geophysics and Planetary Physics, University of California, Santa Cruz, Santa Cruz, California, USA.
[3]Institute of Tibetan Plateau Research, Chinese Academy of Sciences, Beijing, China.
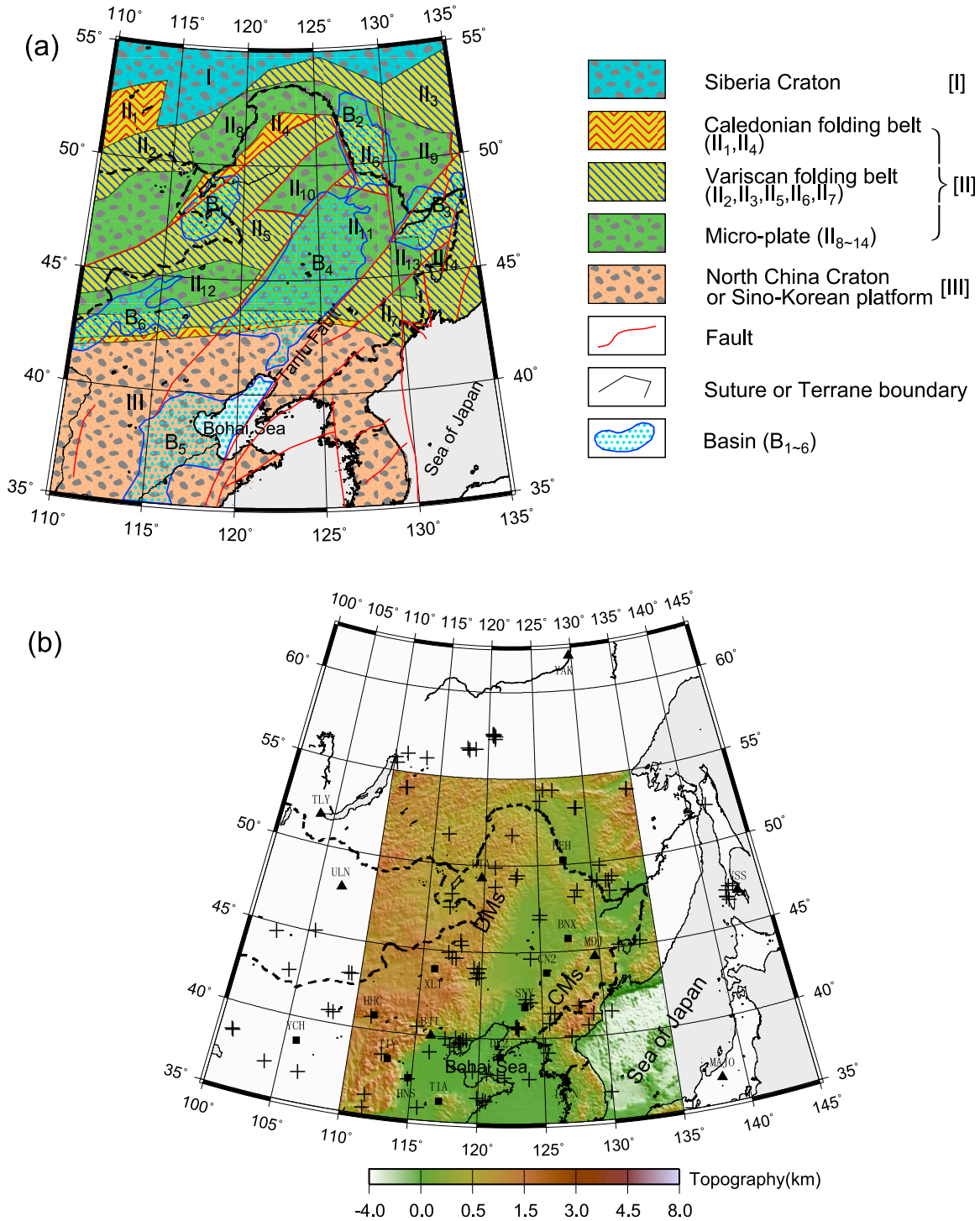
Figure 1. (a) Geotectonics in and around Northeast China (revised from *Xie* [2000] and *Ge and Ma* [2007]). The region includes three large-scale plates: the Siberian Craton (I), the Northeast China Collage (II), and the North China Craton (III). The Collage plate (II) is composed of folding belts (II$_{1-7}$) and microplates (II$_{8-14}$). Also shown in Figure 1a are six sedimentary basins: (B$_1$) Hailaer Basin, (B$_2$) Bureya Basin, (B$_3$) Sichote Basin, (B$_4$) Songliao Basin, (B$_5$) Bohai Bay Basin, and (B$_6$) Xilinhaote Basin. (b) An extended map showing locations of the China National Digital Seismic Network (filled squares) and Global Seismographic Network (triangles) stations and epicenters (crosses) of regional events used in this study. The study region is highlighted by colored topography, with two major volcanic areas, the Daxinganling Mountains (DMs) and the Changbaishan Mountains (CMs), labeled.

Table 1. Codes and Locations of the Stations Used in This Study[a]

Code	Latitude (°N)	Longitude (°E)	Elevation (m)	Network
BNX	45.739	127.405	198	CNDSN
HEH	50.250	127.410	168	CNDSN
HHC	40.849	111.564	1169	CNDSN
SNY	41.828	123.578	54	CNDSN
XLT	43.893	116.074	1020	CNDSN
DL2	38.906	121.628	62	CNDSN
CN2	43.801	125.448	223	CNDSN
TIA	36.211	117.124	300	CNDSN
TIY	38.430	113.017	900	CNDSN
HNS	37.418	114.708	20	CNDSN
YCH	38.609	105.933	1545	CNDSN
MDJ	44.616	129.592	200	GSN
INCN	37.483	126.633	419	GSN
BJT	40.018	116.170	137	GSN
HIA	49.267	119.742	610	GSN
YAK	62.031	129.681	91	GSN
TLY	51.681	103.644	579	GSN
ULN	47.865	107.053	1615	GSN
YSS	46.958	142.761	98	GSN
MAJO	36.543	138.207	405	GSN

[a]CNDSN, China National Digital Seismic Network; GSN, Global Seismographic Network.

craton, and the Yangzi plate. During the Cenozoic, tectonic events frequently occurred in this region [*Chi*, 1988; *Cai et al.*, 2002; *Ma et al.*, 2003; *Ge and Ma*, 2007]. Figure 1a shows a geological map of Northeast China including the major faults, folding belts, and basins. Figure 1b illustrates the investigated area (highlighted by colored topography), with the two major mountain areas, the Changbaishan Mountains (CMs) and Daxinganling Mountains (DMs), labeled.

[5] Investigating the Q_{Lg} distribution in Northeast China and its vicinity can provide new insight into the regional geology. Earlier works addressing *Lg*-wave attenuation in this region were conducted by *Jin and Aki* [1988], who obtained a 1 Hz coda Q map in China. By using analog records *Ge et al.* [1989] and *Huang et al.* [1990] obtained an average Q_{Lg} of 500 in Northeast China. *Mitchell et al.* [1997, 2008] investigated the *Lg* coda Q variations across Eurasia and obtained a large-scale 1 Hz coda Q image. Using the power-law attenuation model $Q(f) = Q_0 f^\eta$, where Q_0 is the 1 Hz Q and η is an index, *Xie et al.* [2006] measured the Q_{Lg} in eastern Eurasia and derived a tomographic model for Q_0 with a resolution of between 4° and 10°. They revealed the relation between the Q_{Lg} distribution and the deformed regions of the regional fault systems. *Phillips et al.* [2005] used the amplitude ratio technique to image the Q_{Lg} in central and eastern Asia. On average, their image is resolved to 2.5°, with the resolution peaking at 1.5° in the best covered areas. Using the M_L amplitude catalog, *Pei et al.* [2006] obtained a laterally varying 1 Hz Q model within the crust of northern China. *Chung et al.* [2007] studied the 1 Hz Q_{Lg} around the Korean Peninsula including part of Northeast China and the Sea of Japan. *Ford et al.* [2009] compared the Q_{Lg} images in the Yellow Sea and North Korea region obtained using different methods. In this study, we use a larger regional data set to constrain the Q_{Lg} and focus our attention on Northeast China and its vicinity. Without applying any a priori assumptions on the frequency dependence of the attenuation model or source spectra, we invert

the Q_{Lg} at discrete frequencies. With improved spatial resolution and a broad frequency band, the new attenuation model is expected to directly benefit studies of the regional geology, characterization of the sources of regional events, and estimation of the attenuation of strong-motion waves.

2. Data

[6] Our data set includes 1720 broadband vertical-component digital seismograms recorded at 20 stations from 125 regional events between October 1995 and August 2007. The code names, locations, and affiliations of seismic stations are obtained from *Shen et al.* [2008] and listed in Table 1. Nine of these stations belong to the Global Seismographic Network (GSN) operated by the U.S. Geological Survey (USGS) and the Incorporated Research Institutions for Seismology (IRIS) Consortium. The remaining 11 stations are from the China National Digital Seismic Network (CNDSN) operated by the China Earthquake Network Center (CENC). Both the GSN and the CNDSN stations are equipped with broadband instruments that have nearly flat velocity response curves from approximately 0.03 to 8.0 Hz and a sampling rate of 20, 40, or 50 points per second. The event parameters are listed in Table 2. Illustrated in Figure 1b are the station locations (triangles for GSN stations and squares for CNDSN stations) and the epicenters (crosses) used in this study.

[7] The depth of the Moho discontinuity in this region varies from 29 km under the Bohai Bay Basin to approximately 50 km under the northern DMs [e.g., *Zhang et al.*, 2002; *Li and Yuan*, 2003; *Gao et al.*, 2005]. We choose regional events with focal depths shallower than the Moho discontinuity to ensure that they are crustal events. Events with magnitudes between m_b 3.0 and m_b 6.0 are selected, as we avoid the complexity from rupture processes of larger events. A minimum epicentral distance of 192 km is selected to guarantee full crustal-sampling development of the *Lg* phase. We inspect individual traces to remove data that are saturated, are noisy, or have incorrect timing. Although this process reduces the number of useful data, a reasonable-sized data set is still obtained. Figure 2 plots the number of events versus distance and the number of records per event.

[8] To illustrate the data quality, Figure 3 shows the observed seismograms from an earthquake that occurred on 24 March 2004. The waveforms are the normalized vertical ground velocities, with their maximum amplitudes (μm/s) listed to the left of individual traces. The numbers on traces indicate apparent group velocities (km/s). Note that the *Lg* waves arrive at a typical group velocity of 3.5 km/s. High-frequency *Lg* waves are more emphasized at short epicentral distances. They tend to be depleted at longer ranges, indicating the importance of short-distance stations in obtaining high-quality high-frequency signals. The inset map in Figure 3 shows the great circle paths corresponding to this event.

3. Methodology

[9] Commonly used methods for *Lg*-wave Q inversion include simultaneous inversion of source and attenuation, the two-station or reversed two-station method, and the source pair/receiver pair method. For *Lg* coda waves the coda normalization and coda-source normalization [e.g., *Ford et al.*,

Table 2. Parameters of the Events Used in This Study

Contributor	Epicentral parameter						Inverted source parameter	
	Date (yyyy/mm/dd)	Time (UTC)	Latitude (°N)	Longitude (°E)	Depth (km)	Magnitude (mb)	Seismic moment M_0(N m)	Corner frequency f_c (Hz)
ISC	1995/10/05	22:26:55.39	39.727	118.531	8.6	4.0 4.5 4.6 4.9 5.1	7.36 ± .37E+15	1.08 ± .07
ISC	1998/04/14	02:47:50.01	39.595	118.577	23.0	4.2 4.6 4.3 5.1	4.67 ± .24E+15	1.01 ± .07
ISC	1998/07/24	23:12:16.10	48.889	131.484	14.3	3.9 4.1 4.2 4.3	1.62 ± .23E+15	1.17 ± .12
ISC	1998/07/24	23:19:39.92	48.903	131.241	11.8	3.7 4.1 4.4 4.5	2.78 ± .25E+15	1.01 ± .10
ISC	1998/09/26	14:16:43.93	42.296	123.668	10.0	3.8 4.2	3.57 ± .41E+14	.88 ± .11
ISC	1998/11/11	17:27:55.36	48.189	133.145	9.0	3.5 4.0 4.1	9.84 ± 1.27E+14	.92 ± .08
ISC	1999/01/20	13:39:52.10	57.517	120.479	28.6	4.1 4.4 4.6 4.7 4.8	2.09 ± .26E+15	.64 ± .08
ISC	1999/01/20	13:27:58.02	57.569	120.476	33.9	4.2 4.6 4.8 4.9 5.0	5.50 ± .31E+15	.50 ± .03
ISC	1999/01/20	12:36:47.21	57.513	120.601	30.8	3.8 4.1 4.5 4.7	2.30 ± .14E+15	.55 ± .04
ISC	1999/04/01	01:59:47.39	39.650	125.161	10.4	3.4 3.5	1.33 ± .19E+14	1.92 ± .31
ISC	1999/08/13	18:36:22.38	48.468	128.538	8.0	4.1 4.4 4.5 4.6	3.05 ± .20E+15	.96 ± .09
ISC	1999/08/14	00:04:37.69	48.114	128.236	44.5	3.7	1.64 ± .23E+14	2.22 ± .36
BJI[a]	1999/09/03	11:23:32.70	48.960	130.410	29.0	—	5.50 ± .67E+14	1.13 ± .11
ISC	1999/12/27	11:27:19.01	40.541	123.070	21.0	3.6	5.17 ± .45E+14	.91 ± .09
ISC	2000/01/11	23:43:56.00	40.546	123.095	5.0	4.5 4.7 4.8 4.9 5.1	1.01 ± .12E+16	.81 ± .09
ISC	2000/01/12	05:00:37.10	40.676	122.850	36.3	4.5	9.84 ± .89E+14	.93 ± .08
ISC	2000/05/14	15:48:50.23	48.982	129.924	5.5	3.7 4.1 4.2 4.4	1.10 ± .12E+15	1.42 ± .17
ISC	2000/05/23	23:44:36.59	40.645	122.855	30.6	3.9 4.1 4.3	6.74 ± .98E+14	1.43 ± .19
BJI	2000/11/08	13:06:37.10	45.590	118.140	31.0	—	2.31 ± .42E+14	1.93 ± .23
BJI	2000/11/14	08:41:52.50	39.150	125.370	15.0	—	1.13 ± .15E+14	1.55 ± .22
BJI	2000/12/13	09:59:31.20	40.850	125.530	27.0	—	3.71 ± .41E+13	2.71 ± .29
NEIC	2001/03/02	04:29:06.26	40.496	115.033	33.0	4.1	1.06 ± .05E+15	1.86 ± .09
ISC	2001/04/20	04:35:37.75	48.289	117.117	10.0	3.5 3.6	1.71 ± .29E+14	1.88 ± .23
NEIC	2001/05/21	15:35:12.75	36.817	106.507	33.0	4.3	1.86 ± .17E+15	1.17 ± .11
NEIC	2001/06/05	14:56:45.61	40.665	108.322	33.0	4.4	3.10 ± .18E+15	1.39 ± .11
NEIC	2001/08/25	13:21:26.11	35.047	135.654	23.2	5.1	4.00 ± 1.72E+16	.18 ± .03
NEIC	2001/09/01	13:08:11.90	47.360	142.523	10.0	5.7	6.96 ± 1.37E+16	.39 ± .06
SKHL[b]	2001/09/03	03:09:34.00	48.260	133.150	13.0	4.2	2.57 ± .40E+14	.92 ± .12
NEIC	2001/09/19	08:07:26.07	38.043	119.531	33.0	4.4	1.66 ± .15E+15	1.38 ± .14
ISC	2001/10/05	09:20:57.05	45.095	105.585	32.0	4.1 4.3 4.5	1.97 ± .26E+15	1.50 ± .20
ISC	2002/01/27	18:20:31.76	53.681	125.376	16.0	4.2	2.25 ± .49E+14	.78 ± .11
ISC	2002/04/16	22:52:38.63	40.658	128.652	10.0	4.1	1.17 ± .09E+15	.73 ± .05
ISC	2002/04/21	19:34:38.61	37.374	114.697	24.0	4.8 5.0	5.23 ± .59E+15	1.20 ± .11
ISC	2002/04/30	03:22:43.56	40.692	122.964	15.0	3.7	4.27 ± .26E+14	1.06 ± .07
BJI	2002/05/05	10:02:24.90	40.060	127.240	15.0	—	4.00 ± .52E+13	1.74 ± .21
BJI	2002/06/13	07:36:03.70	49.260	122.940	20.0	—	9.83 ± 1.02E+13	1.69 ± .15
ISC	2002/06/16	21:58:40.16	40.601	123.007	38.7	3.9 4.0	3.50 ± .26E+14	1.40 ± .12
ISC	2002/08/29	18:32:16.26	49.451	123.067	16.6	3.5 3.6	6.21 ± .60E+14	.97 ± .07
ISC	2002/10/20	15:46:19.95	44.600	117.470	33.0	4.6 4.8	4.08 ± .41E+15	1.08 ± .09
ISC	2002/10/20	15:52:10.54	44.914	117.142	10.0	3.8 4.2	1.51 ± .15E+15	1.28 ± .12
ISC	2002/10/21	00:10:21.67	44.605	117.801	10.0	3.4	2.61 ± .35E+14	1.76 ± .23
BJI	2003/03/30	11:00:44.40	42.050	123.630	28.0	4.3	2.24 ± .23E+14	1.69 ± .19
ISC	2003/03/30	11:10:55.46	37.625	123.856	10.0	4.7	4.70 ± .39E+15	.79 ± .07
NEIC	2003/04/23	13:46:08.32	39.894	117.328	33.0	4.1	3.27 ± .21E+14	2.61 ± .24
NEIC	2003/04/23	18:39:19.17	39.532	117.705	47.5	4.3	7.44 ± .58E+14	1.46 ± .09
BJI	2003/05/03	12:35:24.70	42.100	124.040	21.0	—	1.79 ± .22E+14	.78 ± .06
BJI	2003/05/07	11:34:16.50	37.870	121.450	10.0	—	2.43 ± 1.11E+14	.73 ± .21
ISC	2003/05/22	08:48:46.88	39.446	118.060	10.0	3.6	2.79 ± .22E+14	2.39 ± .18
ISC	2003/06/01	02:49:17.28	49.800	130.794	7.0	3.7 3.8 4.0	5.10 ± .51E+14	1.27 ± .11
BJI	2003/06/05	10:35:55.40	36.300	120.580	28.0	—	6.75 ± .43E+14	.94 ± .06
ISC	2003/06/05	23:18:42.55	36.477	119.940	33.0	3.7 3.8	1.16 ± .33E+14	1.39 ± .28
ISC	2003/06/08	01:56:48.46	35.409	111.605	14.0	—	1.31 ± .22E+14	1.55 ± .23
ISC	2003/06/10	03:23:20.18	40.732	111.340	22.8	3.7 4.3	7.67 ± .70E+14	2.14 ± .29
BJI	2003/06/12	09:33:59.40	36.360	120.370	15.0	4.0	5.37 ± 1.38E+14	.75 ± .11
SKHL	2003/06/14	14:10:09.70	49.110	131.830	7.0	—	2.13 ± .16E+14	.86 ± .05
ISC	2003/06/18	14:24:31.50	47.533	116.985	16.2	3.9 4.4	1.26 ± .07E+15	1.52 ± .13
ISC	2003/06/21	12:13:09.36	39.691	118.368	16.0	3.7	3.14 ± .12E+14	2.12 ± .14
ISC	2003/07/02	07:44:08.09	36.995	103.944	34.4	4.3 4.5 4.6	5.24 ± .66E+15	.76 ± .06
ISC	2003/07/18	14:03:06.81	53.953	134.323	10.0	3.9 4.0	2.12 ± .14E+15	.80 ± .06
BJI	2003/08/03	23:49:10.00	41.350	130.580	15.0	—	1.54 ± .16E+14	1.38 ± .11
ISC	2003/08/16	10:58:40.76	43.813	119.658	8.8	5.4 5.5 5.8	5.23 ± .49E+16	.68 ± .03
BJI	2003/08/16	11:59:51.30	43.770	119.670	16.0	—	1.50 ± 1.01E+14	1.23 ± .56
BJI	2003/08/17	05:24:23.70	44.040	119.800	20.0	—	1.26 ± .08E+14	2.43 ± .18
BJI	2003/08/17	16:33:22.50	37.930	120.610	17.0	—	2.46 ± .25E+14	.89 ± .07
ISC	2003/08/25	18:48:32.14	38.642	112.528	10.0	3.8 4.1	5.56 ± .60E+14	1.82 ± .20
BJI	2003/09/09	05:09:29.60	44.060	119.350	19.0	—	1.67 ± .17E+14	1.73 ± .22
ISC	2003/09/16	11:24:53.67	56.075	111.296	18.3	5.2 5.3	1.23 ± .23E+17	.32 ± .04
ISC	2003/10/07	15:27:27.80	45.240	133.597	49.4	4.4 4.5	3.20 ± .22E+15	.54 ± .04
ISC	2003/10/09	15:53:29.88	41.435	125.982	8.0	—	1.65 ± .23E+14	1.60 ± .18

Table 2. (continued)

	Epicentral parameter						Inverted source parameter	
Contributor	Date (yyyy/mm/dd)	Time (UTC)	Latitude (°N)	Longitude (°E)	Depth (km)	Magnitude (mb)	Seismic moment M_0(N m)	Corner frequency f_c (Hz)
BJI	2003/10/10	13:34:27.80	41.430	125.650	15.0	—	2.82 ± .65E+14	.82 ± .13
ISC	2003/10/16	21:19:20.01	53.927	134.389	10.0	4.3 4.4 4.5	1.72 ± .15E+15	.95 ± .11
ISC	2003/10/17	01:38:30.75	43.534	119.820	10.0	3.8 4.3	6.87 ± .46E+14	1.67 ± .11
ISC	2003/10/25	12:41:35.20	38.396	100.956	9.0	—	4.79 ± .19E+17	.29 ± .02
ISC	2003/10/25	13:25:21.87	38.340	101.058	0.8	5.0 5.1	7.51 ± 2.90E+16	.24 ± .05
CENC[c]	2003/11/13	02:35:10.00	34.780	103.930	10.0	5.2	8.30 ± 1.95E+16	.23 ± .03
ISC	2003/11/14	21:43:18.57	39.887	118.704	10.0	4.0	4.21 ± .21E+14	2.16 ± .14
ISC	2003/11/25	05:40:30.54	36.164	111.662	10.0	4.6 4.8 4.9	5.44 ± .57E+15	1.00 ± .09
ISC	2004/01/16	19:08:31.92	53.184	129.032	10.0	4.0 4.2 4.3 4.4 5.2	1.21 ± .12E+16	.62 ± .08
ISC	2004/01/17	05:09:30.54	54.286	126.702	9.0	3.8 4.6	3.01 ± .42E+14	1.09 ± .12
ISC	2004/01/20	08:34:12.05	39.858	118.982	23.4	4.5	2.04 ± .14E+15	1.25 ± .10
ISC	2004/01/25	19:46:27.44	53.190	128.883	9.0	4.0 4.2 4.8	2.84 ± .25E+15	.82 ± .08
BYKL[d]	2004/03/22	03:49:59.60	56.680	118.640	16.0	4.4	2.05 ± .36E+14	.91 ± .12
ISC	2004/03/24	01:53:47.50	45.349	118.209	18.0	5.5 5.6 5.7 5.8	5.17 ± .34E+16	.69 ± .03
ISC	2004/03/24	19:55:49.18	54.316	125.723	10.0	4.0 4.1 4.3 4.9	9.05 ± .54E+14	1.09 ± .09
NEIC	2004/05/26	23:56:52.11	54.124	111.714	10.0	4.6	4.30 ± .46E+15	.62 ± .06
NEIC	2004/05/27	00:36:42.74	54.106	111.643	10.0	4.1	6.20 ± .97E+14	1.08 ± .17
NEIC	2004/05/29	10:14:28.44	36.634	129.928	29.2	5.3	5.30 ± .75E+16	.29 ± .03
NEIC	2004/05/30	02:52:12.28	47.311	142.120	13.7	4.9	7.45 ± .66E+15	.73 ± .07
ISC	2004/06/28	14:22:44.47	56.592	117.944	4.6	4.6 4.7 4.8	8.66 ± 1.28E+15	.63 ± .08
NEIC	2004/09/16	17:14:37.47	45.137	131.727	10.0	3.9 4.0 4.1	3.64 ± .31E+14	.90 ± .06
BYKL	2004/10/24	04:31:38.60	56.630	117.930	12.0	4.4	3.89 ± .28E+14	.80 ± .05
NEIC	2004/12/16	18:59:14.60	41.804	127.979	10.0	4.0	6.57 ± .56E+14	1.15 ± .10
NEIC	2005/01/02	00:24:37.88	56.723	117.753	13.4	5.2	3.39 ± .54E+16	.48 ± .07
NEIC	2005/01/24	12:22:46.53	51.755	122.584	10.0	4.5	1.12 ± .08E+15	1.55 ± .13
NEIC	2005/02/27	13:27:36.57	40.738	107.909	10.0	4.0	1.13 ± .11E+15	.55 ± .04
ISC	2005/03/08	23:58:36.94	52.163	141.879	10.0	4.9 5.2 5.4	2.00 ± .83E+17	.14 ± .03
CENC	2005/04/09	02:44:18.90	34.040	104.450	10.0	4.9	1.80 ± .34E+16	.40 ± .05
NEIC	2005/05/09	11:02:24.21	37.686	121.966	10.0	4.0	5.29 ± .33E+14	1.42 ± .08
NEIC	2005/07/06	23:10:16.68	48.295	131.473	10.0	4.3	8.99 ± .66E+14	1.06 ± .11
NEIC	2005/07/20	21:54:05.72	43.066	109.017	6.0	5.5	4.12 ± .43E+16	.67 ± .05
NEIC	2005/07/20	18:06:57.44	43.045	109.260	17.8	5.1	1.89 ± .16E+16	.72 ± .05
NEIC	2005/07/25	15:43:36.30	46.892	125.002	10.0	5.0	1.07 ± .13E+16	.91 ± .09
CENC	2005/07/25	15:57:14.80	47.140	125.030	25.0	—	3.69 ± 5.73E+14	1.02 ± .47
NEIC	2005/07/26	12:16:08.93	42.541	104.144	16.0	5.2	4.89 ± 1.24E+16	.40 ± .07
NEIC	2005/09/19	03:27:53.20	49.878	121.003	10.0	4.9	3.12 ± .20E+15	1.27 ± .10
NEIC	2005/11/10	19:29:54.00	57.445	120.537	6.0	5.8	4.01 ± .54E+17	.23 ± .02
NEIC	2005/12/11	15:54:15.90	57.431	120.751	20.0	4.2 5.6 5.7	1.78 ± .41E+17	.29 ± .04
NEIC	2006/01/06	01:56:38.94	51.716	116.413	10.0	4.6	2.70 ± .22E+15	1.27 ± .12
NEIC	2006/03/31	12:23:17.86	44.624	124.122	10.0	4.9	5.62 ± .60E+15	1.00 ± .07
NEIC	2006/04/09	09:23:59.66	35.752	115.591	10.0	4.4	3.12 ± .31E+15	1.23 ± .14
NEIC	2006/05/03	00:26:37.50	48.783	121.049	35.4	3.7	7.87 ± .44E+14	1.72 ± .17
NEIC	2006/05/03	13:53:42.61	39.991	118.153	10.0	3.9	5.87 ± .29E+14	1.45 ± .07
NEIC	2006/05/03	14:02:25.93	39.690	118.469	10.0	4.1	9.03 ± .44E+14	1.54 ± .08
NEIC	2006/07/04	03:56:26.94	39.071	116.153	10.0	5.0	6.29 ± .40E+15	1.04 ± .06
NEIC	2006/07/07	14:12:07.14	44.551	102.352	10.0	5.1	3.03 ± .40E+16	.50 ± .05
NEIC	2006/08/17	15:20:35.02	46.542	141.908	14.0	6.0	1.55 ± .14E+17	.27 ± .03
NEIC	2006/10/09	01:35:28.00	41.294	129.094	0.0	3.6 4.2 4.3	6.71 ± .81E+14	.60 ± .05
NEIC	2006/11/03	06:21:39.28	43.469	119.558	10.0	4.7	1.41 ± .10E+15	1.27 ± .10
NEIC	2006/11/20	00:07:28.37	57.287	120.726	10.0	4.8	2.93 ± .35E+15	.48 ± .04
NEIC	2006/12/04	09:14:04.60	55.769	110.075	10.0	5.1 5.2	1.02 ± .25E+17	.25 ± .04
NEIC	2007/07/04	01:23:24.44	55.474	110.300	10.0	5.3	1.09 ± .17E+17	.27 ± .04
NEIC	2007/08/02	08:06:28.81	46.743	141.733	10.0	5.3	3.40 ± .25E+16	.44 ± .02
NEIC	2007/08/02	05:22:17.69	46.714	141.722	10.0	5.6	2.80 ± .46E+17	.15 ± .02
NEIC	2007/08/02	02:37:42.38	47.116	141.798	5.0	5.3	4.41 ± .45E+17	.13 ± .01
NEIC	2007/08/23	04:49:19.80	55.950	113.381	19.0	5.0	1.28 ± .21E+16	.66 ± .08

[a]Beijing regional network.
[b]Sakhalin regional network.
[c]China earthquake network center.
[d]Baykal regional network.

2008] methods are often used. Limited by the available data, trade-offs are often adopted to simplify the Q_{Lg} inversion. For example, *Xie* [1993] addressed the trade-offs among Q_{Lg}, the source radiation pattern, and the site response. *Ottemöller* [2002] and *Ottemöller et al.* [2002] imaged the

apparent crustal Q_{Lg} in Central America based on similar considerations. However, many researchers [e.g., *Phillips et al.*, 2005] have emphasized the importance of source coupling and site response on attenuation measurement. Here we apply the tomographic method to investigate Q_{Lg}
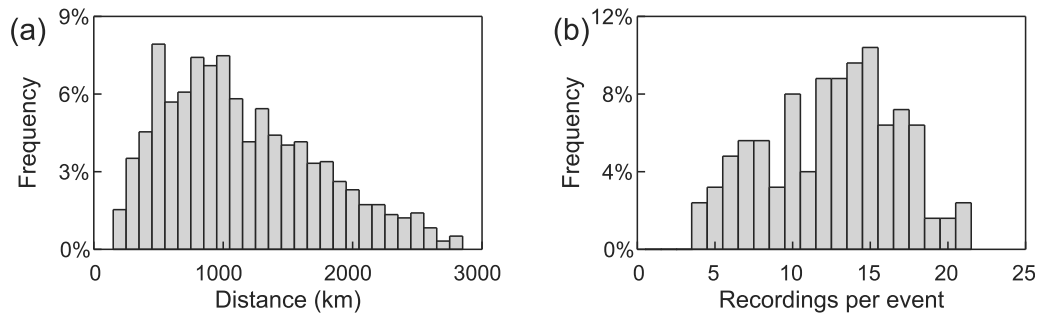
Figure 2. Statistics of the regional data set, with (a) number of rays versus distances and (b) number of records per event.

in Northeast China and the surrounding area. Limited by the available data, the frequency-dependent site response and source coupling are not considered in our inversion. For the same reason, we neglect the effect of radiation pattern and assume that the source is isotropic.

3.1. Data Preprocessing

[10] Following *Xie and Mitchell* [1990], we conduct the following data preprocessing for all available *Lg* waveforms: (1) setting windows for the *Lg* waves and the noise, (2) calculating Fourier spectra for the *Lg* waves and the noise, (3) sampling the spectral amplitudes, and (4) correcting the effect of noise on the signal amplitudes.

[11] *Xie and Mitchell* [1990] suggested a recursive zerophase, fourth-order Butterworth filter with a 1 Hz corner frequency to isolate the corresponding *Lg*-wave train and used it to determine the *Lg*-wave group-velocity window. *Nuttli* [1986] determined the *Lg* window directly from the World-Wide Standard Seismogram Network (WWSSN) short-period (SP) seismograms. Analogously, *Patton and Schlittenhardt* [2005] convolved the broadband waveforms with a WWSSN response to simulate short-period seismograms from which they visually selected the *Lg* group-velocity window. Both methods emphasize the high-frequency content in the *Lg*-wave train. Here we follow *Patton and Schlittenhardt* [2005]. Figure 4 illustrates simulated WWSSN *SP* seismograms for the same event as shown in Figure 3. After visually inspecting all of the seismograms, we set the *Lg* group-velocity window to be either 3.6–3.0 or 3.5–2.9 km/s. The noise series are picked from a time window that has the same length as the *Lg* window and is located immediately before the first-arriving *P* wave [*Zhao et al.*, 2008].

[12] To calculate Fourier spectra for both the *Lg* wave and pre-*P* noise, we add 10% duration intervals both before and after the time windows and apply cosine tapers on the extended portions. A fast Fourier transform (FFT) is then performed on the windowed signals to calculate the spectra. Figure 5 illustrates this process, where Figures 5a and 5b are broadband seismograms with time windows for the *Lg* wave and pre-*P* noise, Figures 5c and 5d are windowed wave trains for the *Lg* wave and the noise series, and Figure 5e shows the amplitude spectra for the *Lg* wave and ambient noise.

[13] To obtain a broadband Q_{Lg} model, we measure the *Lg* spectral amplitudes at 58 frequencies distributed log evenly between 0.05 and 10.0 Hz. At each frequency *f* the corresponding spectral amplitude is calculated using a root

mean square method, $A(f) = \sqrt{1/(M-1)\sum_{i=1}^{M}[A(f_i)]^2}$, where $A(f_i)$ is the spectrum directly from the Fourier transform, $f_i \in [f_1, f_2]$, f_1, and f_2 can be determined by $\log_{10}(f) - \log_{10}(f_1) = \log_{10}(f_2) - \log_{10}(f) = 0.02$, and *M* is the number of data points between f1 and f2. Figure 5e shows 58 discrete amplitude values calculated between 0.05 and 10.0 Hz for both *Lg* waves and the noise series.

[14] To conduct the noise correction we assume that the recorded seismogram in the *Lg* window is a superposition of the *Lg* wave and noise. By further assuming that the two are uncorrelated, we can obtain the *Lg*-wave spectral amplitude from the raw data and the noise amplitude using $A_S^2(f) = A_O^2(f) - A_N^2(f)$, where *A* is the amplitude and the subscripts *S*, *O* and *N* denote the true signal, the observed raw data, and the noise, respectively. From spectral amplitudes of the signal and the noise we can calculate signal-to-noise ratios at individual frequencies, which are shown in Figure 5f. By introducing a threshold of 2.0 for the signal-to-noise ratio (dashed line in Figure 5f), we can judge the quality of the *Lg*-wave spectrum. Illustrated in Figure 5g is the noise-corrected *Lg*-wave spectrum where points below the threshold have been dropped.

[15] Owing to the strong attenuation of high-frequency signals in the crustal waveguide, the amplitude of the high-frequency *Lg* decays rapidly and tends to be affected by noise at large distances. To examine the quality of these data, amplitude-distance curves for individual frequencies are calculated. From these curves we find that spectral amplitudes beyond certain epicentral distances are sometimes suspicious. To eliminate their effect we set up a truncation distance depending on the frequency (Table 3). For a given frequency the data collected from stations beyond the truncation distance are excluded.

3.2. *Lg Q* Tomographic Scheme

[16] We design a tomographic method to simultaneously invert the Q_{Lg} and the source function frequency by frequency. This method is similar to those used in the seismic velocity tomography and is reported in the Appendix. To construct the inversion system we assume that the *Lg* wave propagates in the crustal waveguide along the great circle path between the source and the station. Additionally, we assume that the Q_{Lg} can be expressed as $Q = Q(x,y,f)$, where (x,y) is the surface location. The inversions are independently conducted for individual frequencies. We do
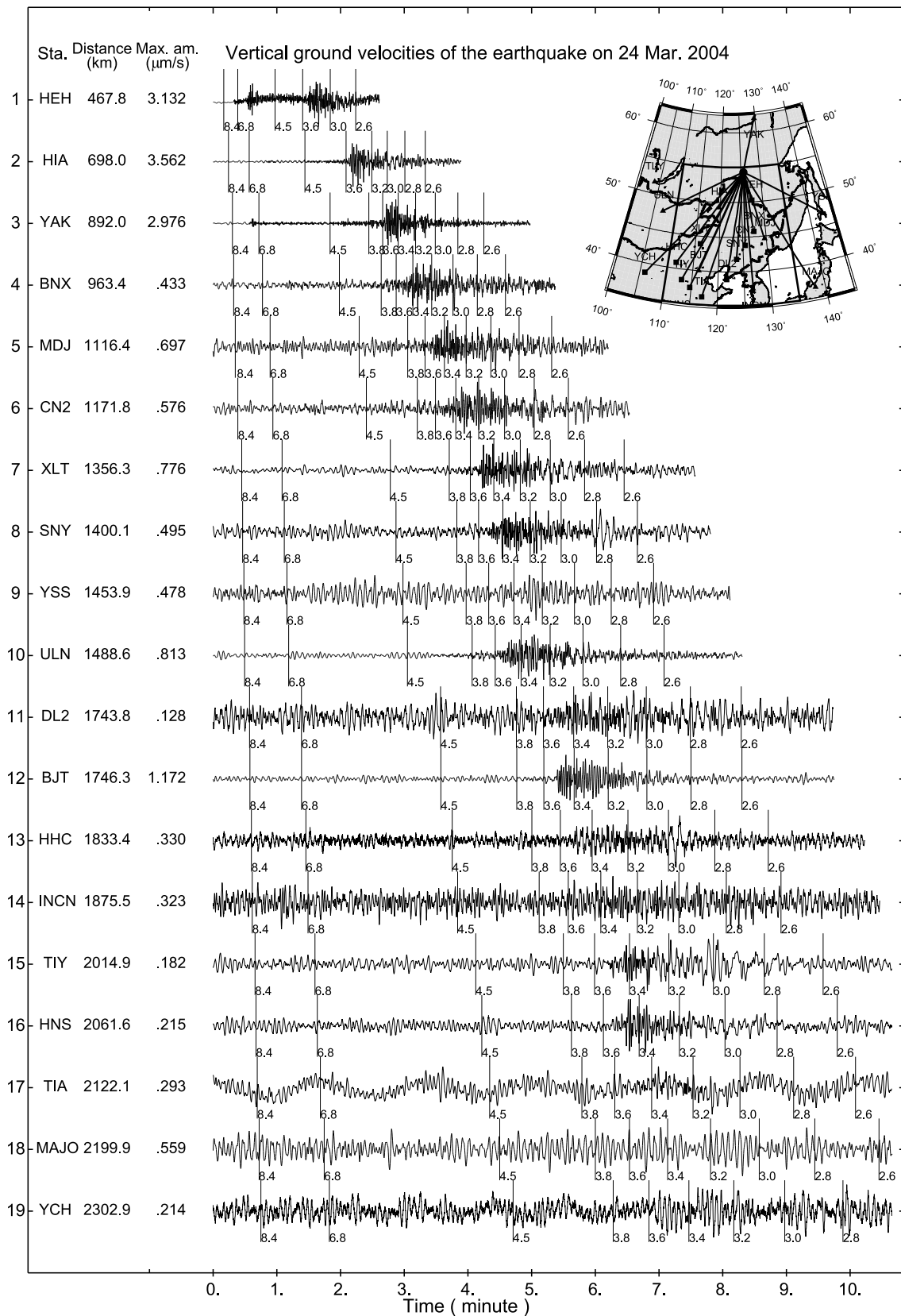
Figure 3. Sample records from earthquake 20040324. Shown here are normalized vertical ground velocities ordered according to their epicentral distances. Station names and maximum amplitudes as micrometers per second are listed at the left. Numbers on the waveforms indicate apparent group velocities. Inset: map showing the great circle paths from the epicenter to stations.
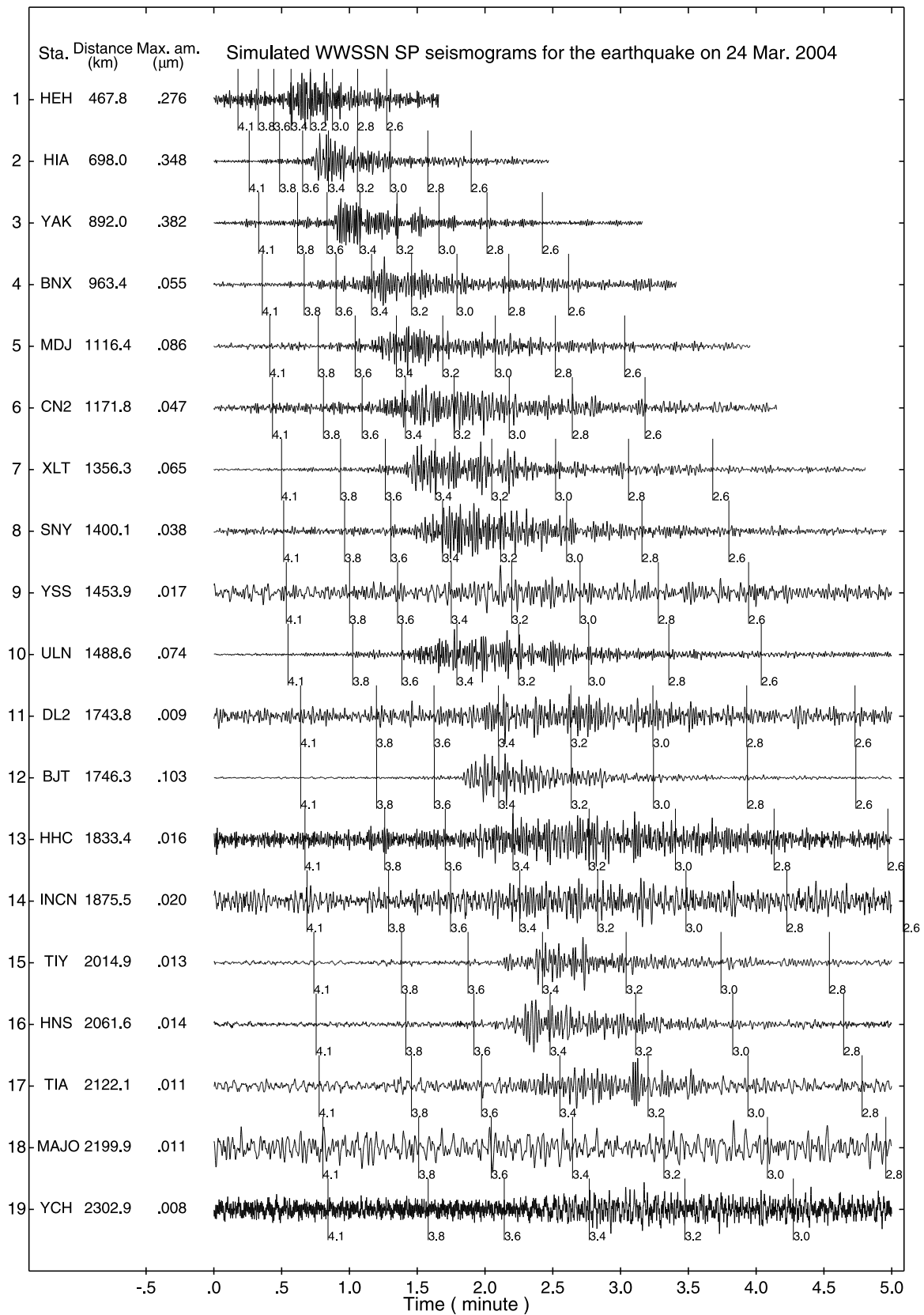
Figure 4. Simulated World-Wide Standardized Seismograph Network short-period vertical displacement seismograms for the same event shown in Figure 3. Maximum amplitudes are in micrometers.

Figure 5. Data processing procedure for *Lg* waves. (a) Original seismogram, (b) velocity record after deconvolving with the instrument response, (c, d) windowed *Lg* phase and pre-*P* noise, (e) *Lg*-wave and noise spectra, (f) signal-to-noise ratio, and (g) *Lg*-wave spectrum. Note that the data points have been dropped where the signal-to-noise ratio is below the threshold of 2.0.

not assume any a priori frequency dependence for Q_{Lg} or the source function. The relationship between the Q value and the observed spectral amplitude is nonlinear. We use perturbation theory to linearize the relationship among the Q model, the source function, and the observed *Lg*-wave spectrum. Finally, an iterative method is used to solve the problem.

[17] In the Appendix, we obtain a linear system,

$$\mathbf{H} = \mathbf{A} \cdot \delta\mathbf{Q} + \mathbf{E} \cdot \delta\mathbf{U}, \tag{1}$$

where $\mathbf{H}$ is a vector composed of residuals between the observed and the synthesized *Lg* spectra, $\delta\mathbf{Q}$ is a vector composed of the perturbations of the Q model, matrix $\mathbf{A}$ sets up the relationship between Q perturbations and the observed *Lg*-wave spectra, $\delta\mathbf{U}$ is a vector composed of the perturbations of source terms, and matrix $\mathbf{E}$ sets up the relationship between the source perturbation and the observed *Lg*-wave spectra. Detailed expression of equation (1) is provided in the Appendix.

[18] To start the calculation we use a unit source function and a constant initial Q_{Lg} model. On the basis of previous work in this region, for example, *Xie et al.* [2006] and *Zhao et al.* [2008], the initial Q model is prescribed using $Q(f) = Q_0 \cdot f^\eta$, with $Q_0 = 420$ and $\eta = 0.15$. At each step we solve for perturbations $\delta\mathbf{Q}$ and $\delta\mathbf{U}$ by minimizing the vector $\mathbf{H}$. These perturbations are used to update the Q_{Lg} model and source function. We iterate this process until satisfactory convergence is obtained. By inverting independently for all frequencies we obtain the frequency-dependent Q_{Lg} model and the source functions.

3.3. Resolution Test

[19] The resolution and covariance matrixes are often used for assessing the resolving power of an inversion system [e.g., *Crosson*, 1976; *Phillips et al.*, 2005; *Phillips and Stead*, 2008]. However, for a large-scale inversion, the calculation is often time-consuming. Alternatively, the checkerboard test method has been used in travel-time tomography [e.g., *Zelt*, 1998; *Morgan et al.*, 2002; *Pei et al.*, 2007], waveform tomography [*Rao et al.*, 2006], and imaging of regional seismic propagation efficiency [e.g., *Calvert et al.*, 2000; *Al-Damegh et al.*, 2004; *Pei et al.*, 2006]. *Xie* [2006] discussed the resolving power of Q tomography and argued that the checkerboard resolution test used in velocity tomography yields a less satisfactory result in Q tomography. We adopt the checkerboard test method in our Q_{Lg} tomography for resolution analysis. Bearing in mind that the signal-to-noise ratios vary between frequencies, the available data points are different, resulting in different resolutions at different frequencies. Therefore, the resolution analyses have to be conducted for individual frequencies.

[20] We first create a Q_{Lg} model by superposing checkerboard-shaped positive and negative perturbations on a

Table 3. Truncation Distances

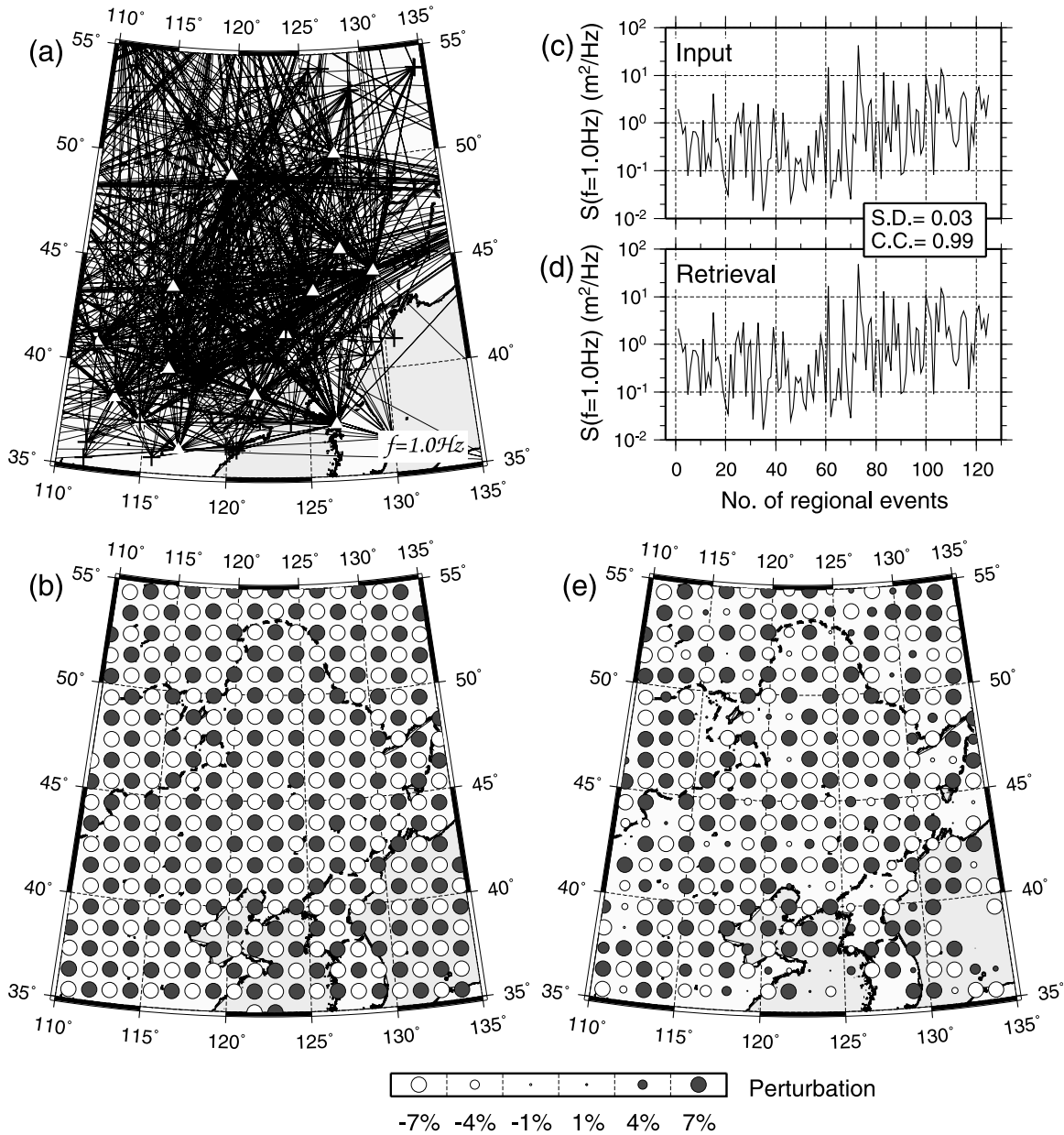| Frequency (Hz)	Distance (km)
<2.0	3000
2.0–2.5	2400
2.5–5.0	1800
5–6.5	1400
>6.5	1000

Figure 6. Resolution analysis at 1 Hz frequency. (a) Event and station geometry and ray paths for 1 Hz *Lg* data, where the crosses and triangles are epicenters and stations, respectively. (b) Initial 1° × 1° checkerboard *Q* model with the alternating positive and negative perturbations. (c, d) Input and retrieved source functions. (e) Retrieved checkerboard *Q* perturbation.

background *Q*. The *Q* perturbation has a constant percentage relative to the background *Q*. Next, we use equation (A1) to generate a synthetic *Lg* spectrum data set. The epicenters and station locations are adopted from the actual observation geometry. The source functions are calculated using equation (A2), with the seismic moment M_0 and the corner frequency f_c estimated from the observed magnitude using empirical relations. At each frequency, only events and stations that actually provide data above the signal-to-noise ratios are used to generate the checkerboard test data. To simulate the noise in the real data a 5% root mean square fluctuation is added to the test data. This synthetic data set is

input to the inversion system and the result is compared to the checkerboard model.

[21] Figure 6 demonstrates the analysis for 1 Hz data. Shown in Figure 6a are 1340 ray paths from all available regional events (crosses) and stations (open triangles). There is denser ray coverage in Northeast China than in surrounding areas. Illustrated in Figure 6b is the 1° × 1° checkerboard test model, which is formed by superimposing ±7% *Q* perturbations on a constant background model of $Q_0 = 420$. Figure 6c gives the 125 preassigned source functions at 1 Hz and Figure 6d shows the retrieved source functions after inversion. The two groups of numbers are highly correlated, indicating that the source functions are properly retrieved.
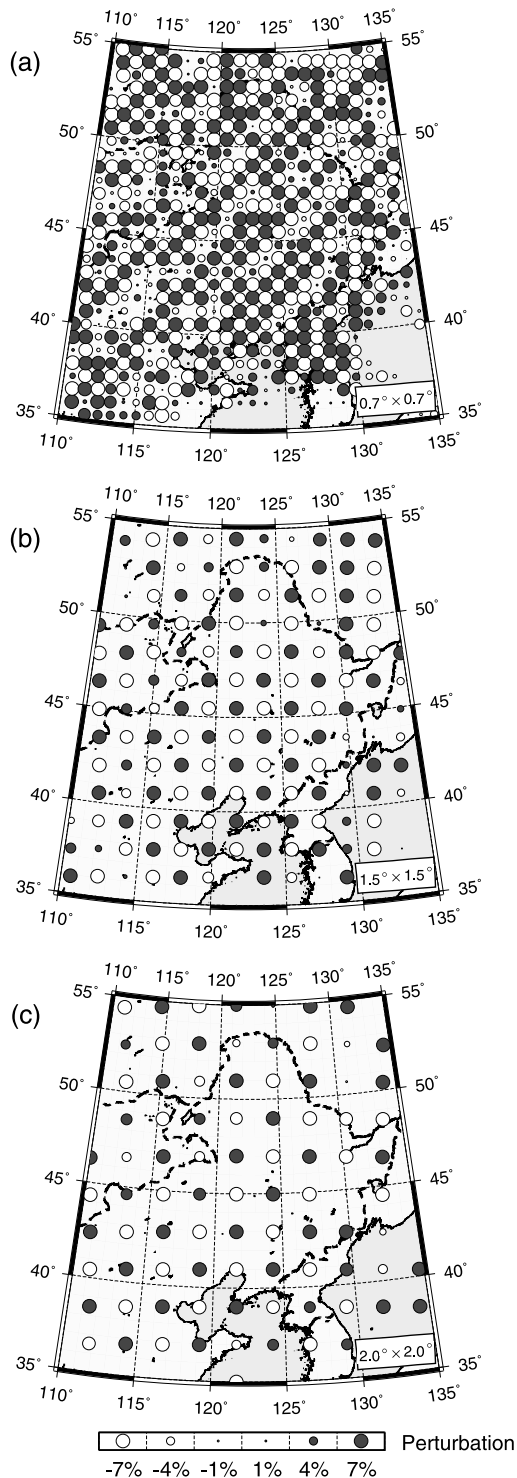
Figure 7. Comparisons of 1 Hz spatial resolutions for different grid sizes. Grid sizes of (a) 0.7° × 0.7°, (b) 1.5° × 1.5°, and (c) 2° × 2°.

Figure 6e illustrates the reconstructed Q model. Comparing Figure 6e with 6b we see that the original checkerboard pattern is mostly resolved in Northeast China compared to surrounding areas and it is consistent with the ray coverage.

[22] For an individual frequency we conduct resolution tests by using a series of checkerboard models. The model

grid sizes vary from 0.5° × 0.5° to 2° × 2°, with an increment of 0.1°. Generally, a fine grid size provides a higher resolution, which is preferred for revealing the correlation between structures and *Lg*-wave attenuation. In contrast, a coarse grid leads to a reliable result but often lacks the details required for characterizing regional geology. Thus, a trade-off must be accepted to balance inversion resolution with reliability. As an example, Figure 7 shows the retrieved 1 Hz checkerboard models with grid sizes of 0.7° × 0.7°, 1.5° × 1.5°, and 2° × 2° for comparison. Clearly, the 0.7° × 0.7° grid causes many regions, even in the central area, to lack resolution. The 1.5° × 1.5° and 2° × 2° grids provide excellent resolving power for almost the entire region except some border areas. However, these coarse grids do not provide enough resolution to reveal attenuation distributions in some basin-mountain transition areas. The 1° × 1° grid, shown in Figure 6e, appears to have the optimal trade-off between the resolution and the reliability for the 1 Hz *Lg* spectrum data. We perform this resolution analyses for all 58 individual frequencies. Figure 8 summarizes the numbers of available rays versus frequency, with the shading illustrating the estimated resolution for particular frequencies obtained by the resolution analyses.

4. Results

[23] Our inversion estimates the Q_{Lg} distributions in Northeast China and its vicinity at 58 discrete frequencies, along with the source spectra for 125 selected events.

4.1. Q_{Lg} Distributions

[24] Figures 9a, 9c, and 9e illustrate examples of Q_{Lg} distributions at 0.5, 1.0, and 2.0 Hz, along with regional geological structures including major fault systems, sutures, and basins. Shown in Figures 9b, 9d, and 9f are ray coverage and resolution tests at these frequencies. The most prominent feature in the Q_{Lg} models is that the high-frequency Q_{Lg} is generally higher than the lower frequency values. Within the investigated region the Q_{Lg} shows a general trend to increase from south to north and the basins are often characterized by low Q values compared to the relatively high Q values in volcanic mountain areas. The active faults delimiting the basin and mountain areas are often related to strong gradients in Q. For example, the Tan-Lu Fault is located on a belt of
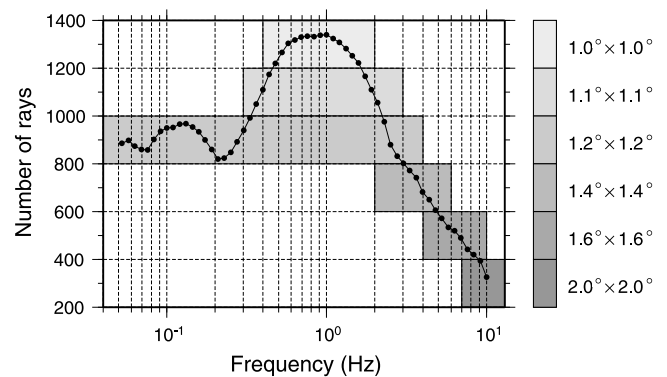

Figure 8. Numbers of rays for frequencies between 0.05 and 10.0 Hz, along with results from resolution analyses.
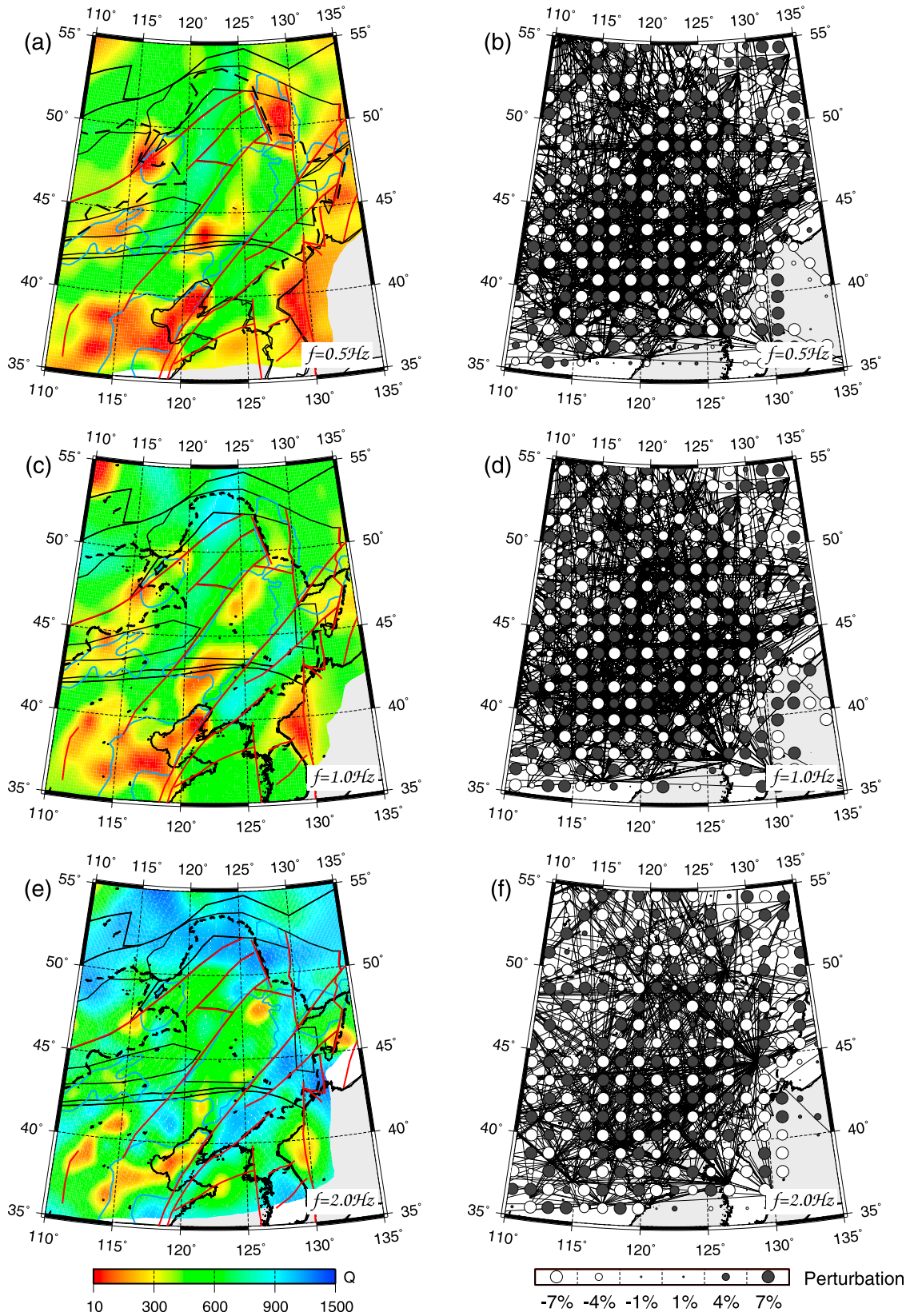
Figure 9. *Lg Q* distributions at frequencies of 0.5, 1.0, and 2.0 Hz, along with their ray coverage and resolution analyses.
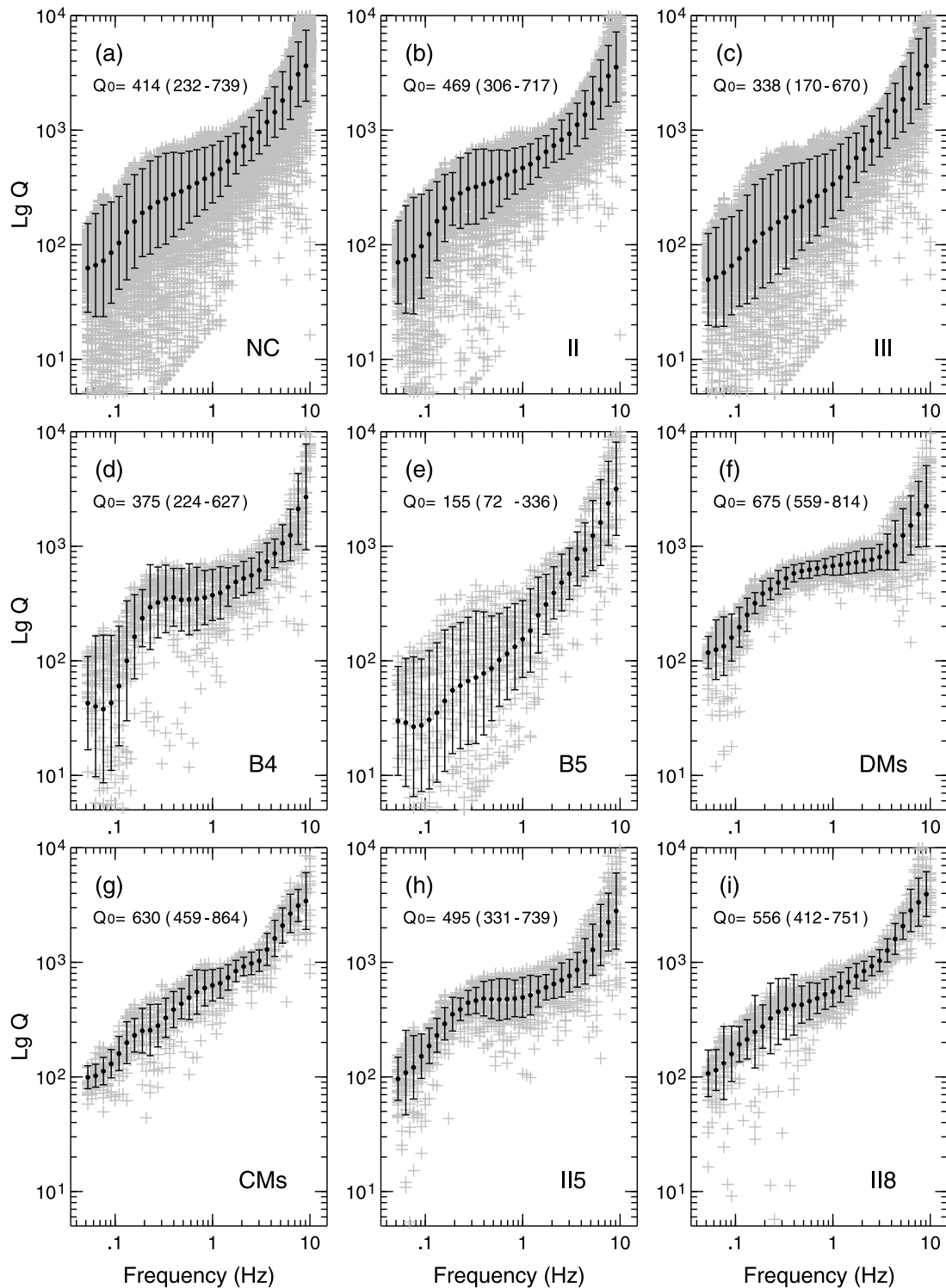
Figure 10. Frequency-dependent *Lg Q* for selected subregions. Gray crosses are directly measured Q_{Lg}. Filled circles with error bars are average values. Q_0 values are labeled in each plot. Standard deviations on a logarithmic scale are converted to Q values and listed in parentheses.

strong Q variation. To the east of this belt the CMs is a volcanic area that has relatively high Q values. To the west of the fault is the Songliao Basin (B4), which bears the largest hydrocarbon deposit in China. During development the basin has experienced a complex process including asthenosphere upwelling, rifting, postrift thermal subsidence, and structural

inversion [*Feng et al.*, 2010]. Relatively low Q values are observed in Songliao Basin (also refer to Figure 1).

[25] To characterize the *Lg*-wave attenuation for different geological formations we investigate regional variations and frequency dependence of Q_{Lg} in different geological units. Figure 10 shows inverted broadband Q_{Lg} versus frequency
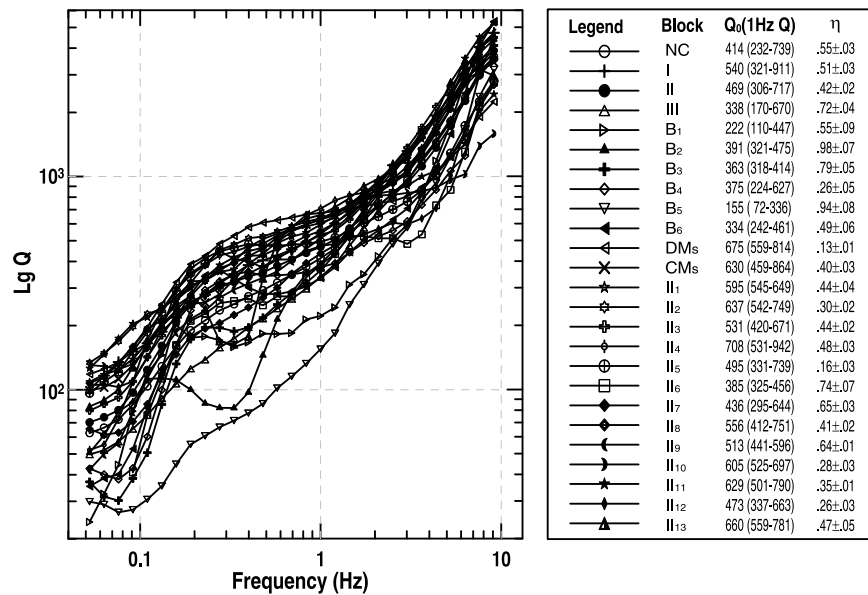
Legend	Block	Q_0(1Hz Q)	η
—○—	NC	414 (232–739)	.55±.03
—+—	I	540 (321–911)	.51±.03
—●—	II	469 (306–717)	.42±.02
—△—	III	338 (170–670)	.72±.04
—▷—	B₁	222 (110–447)	.55±.09
—▲—	B₂	391 (321–475)	.98±.07
—+—	B₃	363 (318–414)	.79±.05
—◇—	B₄	375 (224–627)	.26±.05
—▽—	B₅	155 (72–336)	.94±.08
—◀—	B₆	334 (242–461)	.49±.06
—◁—	DMs	675 (559–814)	.13±.01
—×—	CMs	630 (459–864)	.40±.03
—★—	II₁	595 (545–649)	.44±.04
—✿—	II₂	637 (542–749)	.30±.02
—⊞—	II₃	531 (420–671)	.44±.02
—◆—	II₄	708 (531–942)	.48±.03
—⊕—	II₅	495 (331–739)	.16±.03
—⊟—	II₆	385 (325–456)	.74±.07
—◆—	II₇	436 (295–644)	.65±.03
—◆—	II₈	556 (412–751)	.41±.02
—◀—	II₉	513 (441–596)	.64±.01
—➤—	II₁₀	605 (525–697)	.28±.03
—★—	II₁₁	629 (501–790)	.35±.01
—◆—	II₁₂	473 (337–663)	.26±.03
—▲—	II₁₃	660 (559–781)	.47±.05

Figure 11. Lg Q versus frequency for different geological units. Parameters for power-law Q models obtained by fitting the Lg Q between 0.5 and 1.5 Hz are listed at the right.

in selected subregions. The light gray crosses are directly read from inverted $Q(x,y,f)$ maps (e.g., Figures 9a, 9c, and 9e) within the interested geological formations. We calculate the mean Q_{Lg} values as functions of frequency in different regions. At frequency f the mean value is obtained by averaging all observations within the specific geological unit and between frequencies $f/\sqrt{2}$ and $f \cdot \sqrt{2}$. The mean Q_{Lg} values are shown in each plot by filled circles, along with their standard deviations. Note that the 1 Hz Q_{Lg} in Figure 9c is directly inverted from the 1 Hz Lg data, while here the Q_0 is an average within a frequency band and within a chosen geology unit. Thus the latter is more robust and representative.

[26] Figure 10a shows the observed Q_{Lg} for the entire investigated region, where the average Q_0 is 414, but with a large scatter. The standard deviation is equivalent to Q_0 values of from 232 to 739; this is listed in parentheses. Surrounded by large-scale plates the investigated region is composed of three major units (refer to the caption to Figure 1): Siberian Craton (I), Northeast China Collage plate (II), and North China Craton (III). Figures 10b and 10c show that the average Q_0 for the Northeast China Collage plate is 469 (306–717), and that for the North China Craton is 338 (170–670). The current investigation covers only part of the Siberian Craton, within which the average Q_0 is 540 (321–911) (not shown here). The average Q_0 values reveal a significant difference in crustal attenuation between these first-order geological units, while their relatively large standard deviations indicate strong variations within these units.

[27] We focus our attention on the Northeast China Collage plate, where smaller scale structures include several main sedimentary basins (B₁–B₆) and mountain areas (DMs and CMs). Figures 10d to 10g show some examples from basin and mountain areas. Figure 9 reveals that basins are generally characterized by low Q values, which may result from the strong attenuation in sedimentary stratification or because of the blockage of Lg waves at the edge of basins. The lowest

mean Q_0, 155 (72–336), appears in Bohai Bay basin (B5). On the contrary, high Q_0 values are found in mountain areas, with 675 (559–814) for DMs and 630 (459 to 864) for CMs. The Northeast China Collage plate is composed of approximately a dozen massifs including folding belts and microplates. Shown in Figures 10h and 10i are two examples of the average Q_{Lg} in these massifs. The standard deviations at this level of geology units are usually smaller than those for larger units but their frequency dependence appears to be more complex.

4.2. The Frequency Dependence of Q_{Lg}

[28] Figure 11 summarizes the average Q_{Lg} versus frequency for different geological units in Northeast China and the Korean Peninsula (refer to Figure 1). In general, the mean Q_{Lg} values increase gradually with increasing frequencies of between 0.05 and 1 Hz but rise more steeply above 1 Hz. The low-frequency Q_{Lg} appears to have larger regional variations and a more complex frequency dependence than at high frequencies. By comparing the Q distributions in Figure 9 with the crustal model (Laske, G., G. Masters, and C. Ref (2001), CRUST 2.0: A new global crustal model at 2° × 2°; available at http://igppweb.ucsd.edu/~gabi/crust2.html) in this region, there appears to be some correlation between Q_{Lg} and the crustal thickness. *Zhang and Lay* [1995] investigated the effect of crust thickness on Lg-wave propagation efficiency. They found the crust thickness to be closely related to the maximum number of overtone modes a waveguide can carry, and this number is a dominant factor controlling the Lg-wave propagation efficiency. The number of overtones is proportional to fH [*Zhang and Lay*, 1995], where H is the crust thickness. Although those authors focused on high-frequency Lg waves propagating in continental and oceanic crusts, based on their theory the low-frequency Lg waves should be more sensitive to the crustal thickness. The actual Lg-wave attenuation should be dependent on both the geometrical parameters of the crust waveguide and its physical properties.
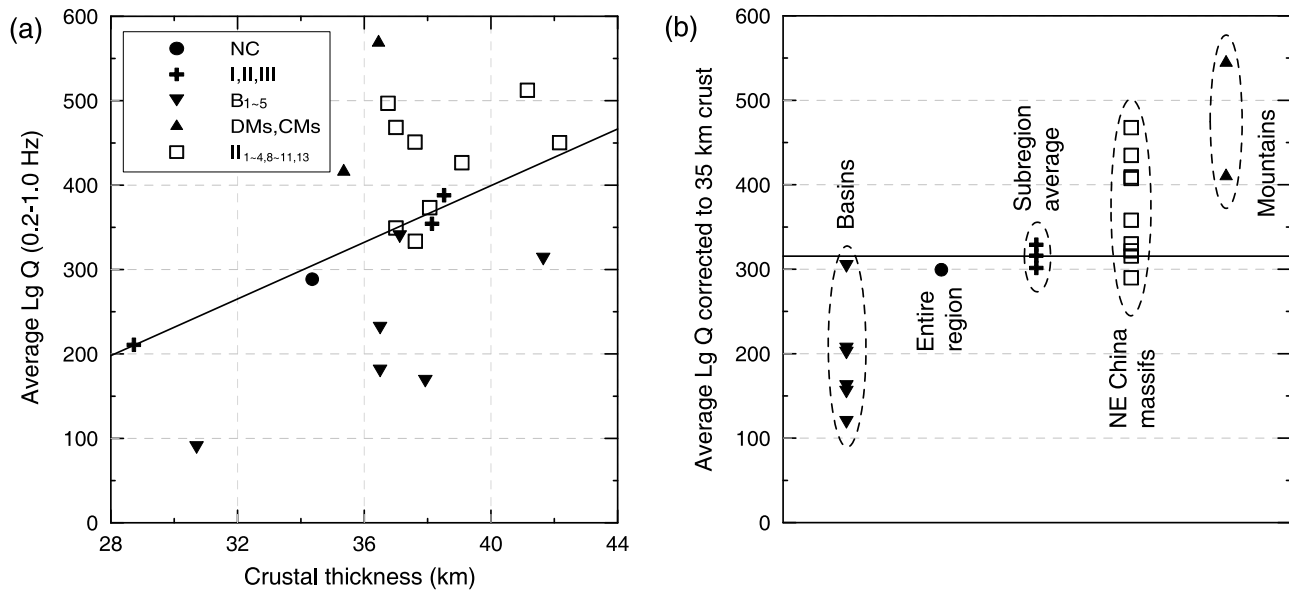
Figure 12. (a) Low-frequency (0.2–1.0 Hz) *Lg Q* values for different geological units versus average crustal thickness. (b) Low-frequency *Lg Q* values after being empirically corrected to 35 km crustal thickness and grouped based on their geology.

We investigate the relationship between the low-frequency Q_{Lg} and the crust thickness and try to separate it from regional Q variations.

[29] Figure 12a shows the average low-frequency Q_{Lg} versus the average crustal thickness for various geological units in Northeast China. The average Q_{Lg} values are calculated using the data in Figure 11 and between 0.2 and 1.0 Hz. The crustal thickness data are from the $2° × 2°$ global crust model CRUST 2.0 (available at http://igppweb.ucsd.edu/~gabi/crust2.html).

[30] The filled circle is the average for the entire investigated region, the three crosses represent the three subregions (Siberian Craton, Northeast China Collage plate, and North China Craton), the triangles are for the mountain areas, and the inverted triangles are for the basins. The squares represent different massifs of Northeast China Collage plates. To prevent ambiguity we exclude the massifs if they partially overlap basin structures. For small geology units the Q_{Lg} values show large variations, indicating that their attenuations are mainly controlled by local geology. However, after averaging for large areas, for example, the crosses for the three major subregions, there appear to be fewer fluctuations. A weak relationship in which the Q_{Lg} values increase with the increase of the crustal thickness, can be seen. The Q_{Lg} values in sedimentary basins show large variations but span a wide crustal thickness range. There appear to be a similar trend with crustal thickness as well. By fitting the points from the three subregional averages (crosses), we obtain a linear relation $Q_{Lg(0.2 – 1.0\ Hz)} = 316 + 16.8 × (H − 35\ km)$. This relationship, the solid line in Figure 12a, describes the weak effect of crustal thickness on the low-frequency Q_{Lg}. To isolate the effect of crust thickness we use this relationship to correct the observed average Q_{Lg} to a reference crust thickness of 35 km and present the result in Figure 12b, where data points have been grouped according to their different geological contexts. Compared to the regional average

the basins have the lowest Q_{Lg} values, which are typically lower than the regional average by 100 to 150. The mountain areas have the highest Q_{Lg} values, which are higher than the regional average by approximately 100 to 200. The average Q_{Lg} values from massifs of the Northeast China Collage plate, after excluding those overlapping with basins, are between 280 and 470 and slightly higher than the regional average. These characteristics provide us with additional information when investigating the links between Q_{Lg} and local geology.

[31] As indicated in Figure 11 the low- and high-frequency Q_{Lg} measurements have different slopes. In some geological units their frequency dependences show more complexities, particularly at low frequencies. These results demonstrate that the frequency dependence of Q_{Lg} is more complex than the commonly adopted power-law Q model, $Q(f) = Q_0 f^{\eta}$, indicating that the power-law model may not be appropriate for a broad frequency range. However, in a narrow band, such a model may still be a useful and convenient approximation. Several authors have indicated that the measurement of η is generally unstable and poorly constrained [e.g., *Xie et al.*, 2006; *Chung et al.*, 2007]. Our Q_{Lg} model is calculated without a power-law assumption and, thus, can be used to examine the behavior of η. Using a linear regression we calculate the slope η from the average Q_{Lg} in Figure 11 and for different frequency bands. The results for three frequency ranges are illustrated in Figure 13, where the vertical coordinate is η (the slope within a specific frequency band), the horizontal coordinate is Q_0, and symbols similar to those used in Figure 12 are used for different geological units. At frequencies of 0.2–1.0 Hz (Figure 13a), the filled circle indicates that the η for average Q_{Lg} in the entire investigated region is close to 0.5. However, the η values for different geology units have different distributions. For basins the distribution of η values is more scattered (ranging between −0.1 and 1.3). This is consistent with their low-frequency
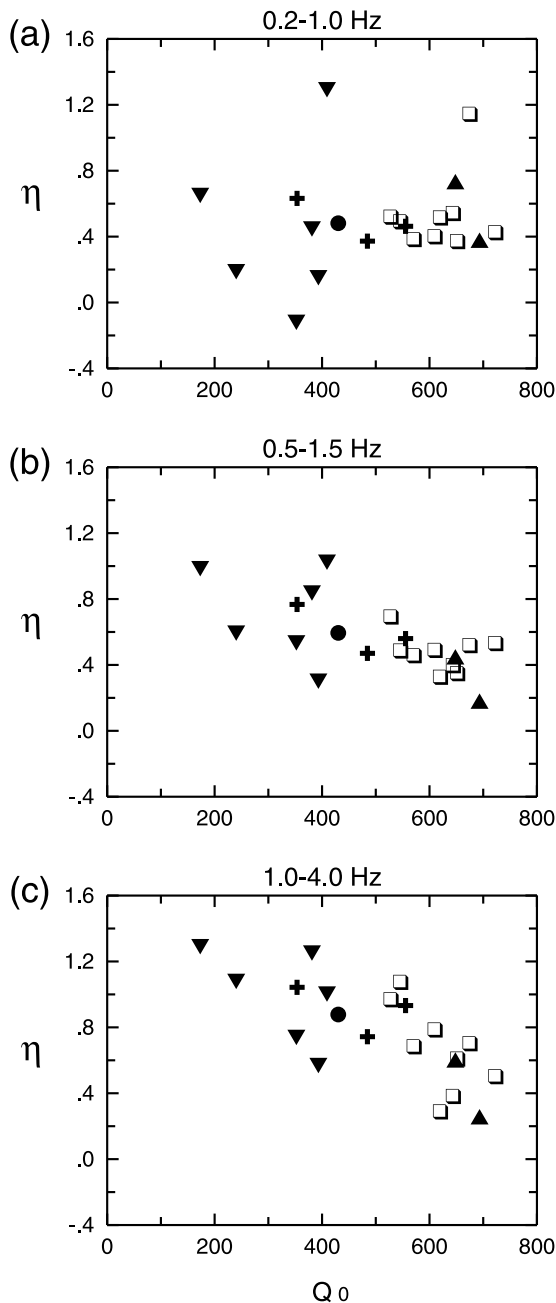
Figure 13. Comparison of distributions of η values (local slopes on Q_{Lg}-frequency curves) for different geological units and for different frequencies: (a) 0.2–1.0 Hz, (b) 0.5–1.5 Hz, and (c) 1.0–4.0 Hz.

behavior shown in Figure 11, where the Q_{Lg} curves from basins often have turning points or even undulations. In contrast, for massifs of the Northeast China Collage plate (excluding those overlapping with basins), η values are mostly distributed between 0.4 and 0.6. For mountain areas η values are between 0.4 and 0.75, although there are only two data points. Figure 13b shows the results for middle frequencies, between 0.5 and 1.5 Hz, which are centered at 1 Hz, and the statistics should be comparable to the conventional narrow-band power-law Q model using a 1 Hz reference frequency. The nominal η is close to 0.55 for the entire investigated

region. Compared to the low-frequency results the η values in basins are less scattered but still distributed between 0.35 and 1.1. The values for massifs of the Northeast China Collage plate and mountain area are distributed from 0.35 to 0.7 and from 0.2 to 0.45, respectively. For the high frequencies (1.0–4.0 Hz) in Figure 13c the distribution of η appears to be more concentrated and tends to decrease with increasing Q_{Lg}. In general, with increasing frequency the η values are shifted upward, a phenomenon shown in Figure 11, where the Q_{Lg}-frequency curves increase in steepness at high frequencies. Our results demonstrate that for a large region, for example, the entire investigated region or the three sub-regions, the Q_{Lg} η values at 1 Hz are between 0.5 and 0.8 and are relatively stable. However, for a small area and within a limited frequency band, the η values may vary to reflect the complex frequency dependence. The aforementioned behavior of η and Q_{Lg} values and regional geology may indicate that the seemingly unstable observations of η values by previous authors [e.g., *Xie et al.*, 2006; *Chung et al.*, 2007] were not simply caused by insufficient data but actually revealed the complex frequency dependence of Q_{Lg}. *Wu and Aki* [1985] reported observations of η and investigated their relation to Q_0 based on the fractal nature of heterogeneities in random models. *Campillo* [1990] summarized several high-frequency Q_{Lg} observations and found that the tectonic regions are often associated with low Q values and strong frequency dependence, while stable areas have high Q values and weak frequency dependence. These results are consistent with ours, particularly at high frequencies.

4.3. *Lg*-Wave Source Spectral Functions

[32] The simultaneous inversion also provides us with the *Lg*-wave excitation functions at discrete frequencies. Figure 14 illustrates source functions for selected events. The crosses represent results for individual frequencies. To obtain the scalar seismic moment M_0 and the corner frequency f_c, we fit the *Lg*-wave excitation spectrum with the ω^2 source model [*Brune*, 1970; *Street et al.*, 1975; *Sereno et al.*, 1988]. With this model, equation (A2) in the Appendix becomes

$$S(f) = \frac{M_0}{4\pi\rho v_S^3 [1 + f^2/f_C^2]}, \tag{2}$$

where ρ and v_S are the average density and shear-wave velocity in the crust, with typical values of 2.7 g/cm^3 and 3.5 km/s for Northeast China [*Jih*, 1998]. Since there is only one explosion source in all 125 regional events, we do not specifically treat this event with an explosion source model [e.g., *Mueller and Murphy*, 1971]. The solid lines in Figure 14 are best-fit source models obtained using the bootstrap method [*Efron*, 1983] and the shaded areas give their standard deviations. The seismic moments and corner frequencies are labeled.

[33] Illustrated in Figure 15 are the inverted and synthetic source models for all 125 events. Although the inversions are conducted independently at individual frequencies, the ω^2 source model is reasonably well fit to the inverted source functions, particularly for frequencies between 0.05 and 5.0 Hz. At very low and very high frequencies there appear to be some deviations, which may be due to insufficient data coverage. The inverted seismic moments and the corner frequencies are listed in Table 2.
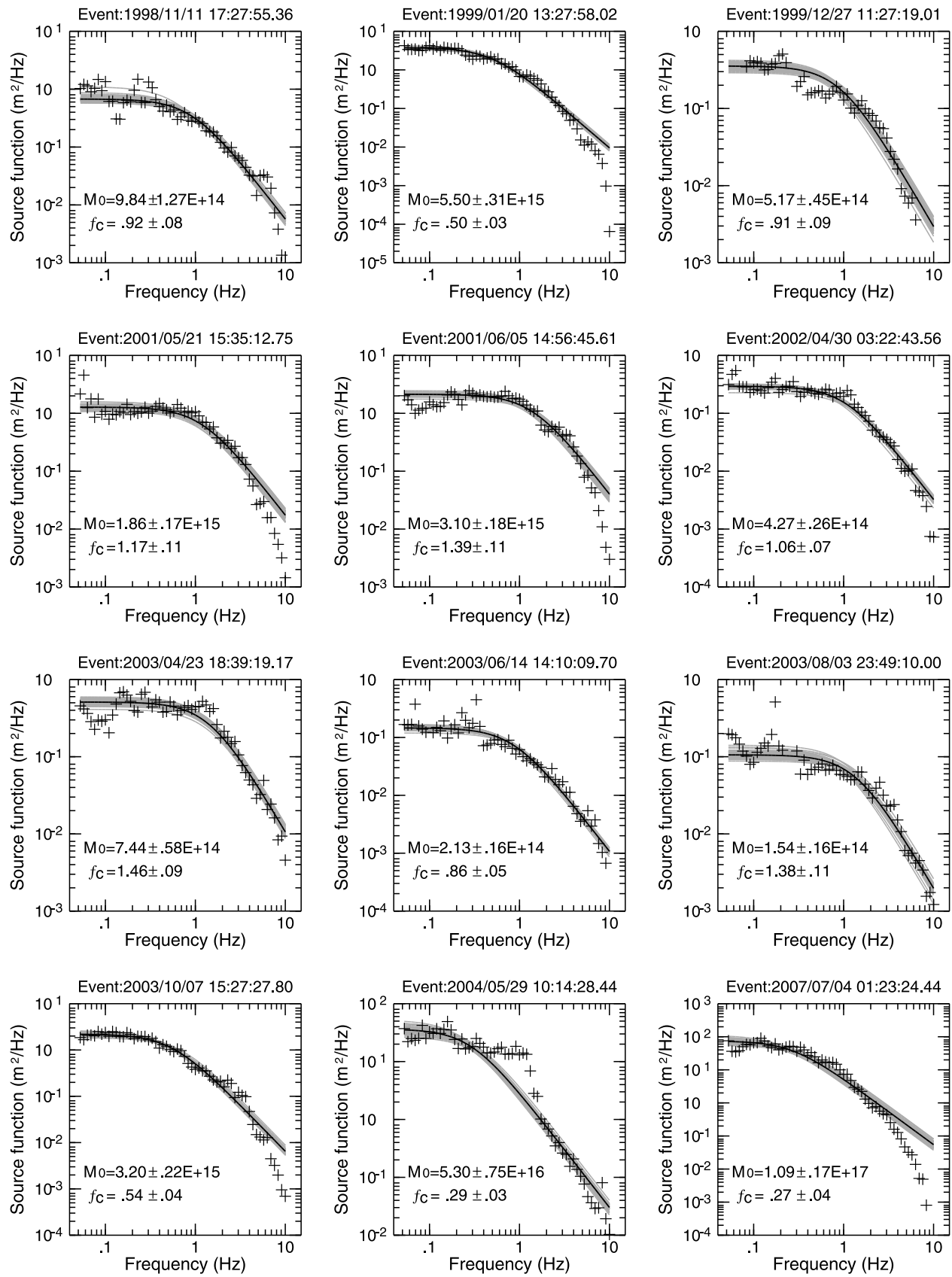
Figure 14. Retrieved *Lg* source excitation spectra for selected regional events. Gray crosses are directly inverted results. Solid lines are best-fit ω^2 source models, and shaded areas are their standard deviations. The resulting M_0 and f_c are labeled in each plot.
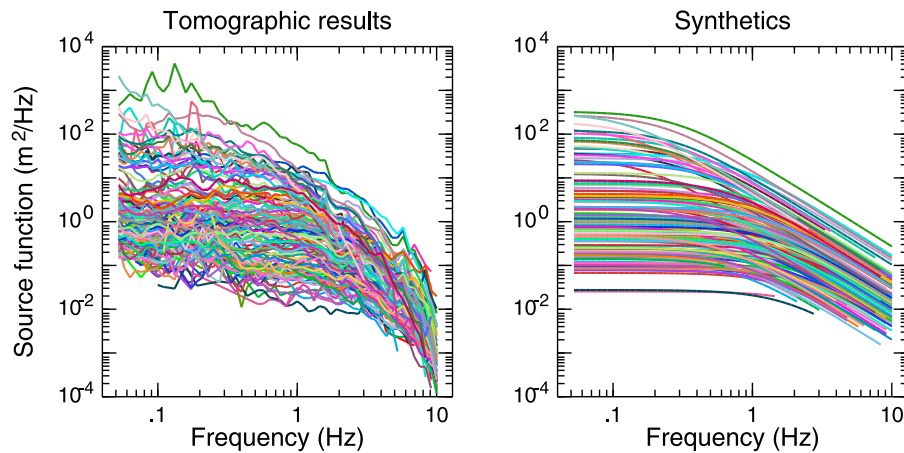
Figure 15. Comparisons between the retrieved (left) and the best-fit (right) source models.

[34] For our simple earthquake source model, the seismic moment M_0 is not only related to the corner frequency f_C but also to the stress drop $\Delta\sigma$ [*Brune*, 1970; *Drouet et al.*, 2005; *Fisk*, 2006],

$$\log_{10}(M_0) = \log_{10}(0.12 \cdot v_S^3 \cdot \Delta\sigma) - 3\log_{10}(f_C). \quad (3)$$

Some investigations have suggested that the $M_0 \propto f_C^{-4}$ scaling is more appropriate than the f_C^{-3} scaling for earthquakes in central Asia and the western United States [*Nuttli*, 1983; *Cong et al.*, 1996; *Mayeda and Walter*, 1996]. *Xie* [2002] observed a similar relation for a group of nuclear and chemical explosions in central Asia. However, *Taylor et al.* [2002] suggested that the departure from −3 scaling can be attributed to a nonconstant stress drop. Assuming that the stress drop is a constant in the investigated region, the current data give a linear relationship between M_0 and the corner frequency f_C,

$$\log_{10}(M_0) = 15.17(\pm 0.05) - 2.82(\pm 0.17)\log_{10}(f_c), \quad (4)$$

where M_0 is in Newton meters. Note that the exponent of the scaling between M_0 and f_C is close to the theoretical prediction. If we take the assumption made by *Taylor et al.* [2002], the stress drop can be calculated from M_0 and f_C using equation (3). The results are shown in Figure 16a, where the stress drops for these regional events are scattered and larger earthquakes appear to have larger stress drops. A regional average value of $\Delta\sigma = 2.81$ bar can be obtained from all events.

[35] Illustrated in Figures 16b is the relationship between M_0 and the body-wave magnitude m_b reported by different regional seismic networks. A linear regression gives the following equation:

$$\log_{10}(M_0) = 10.20(\pm 0.24) + 1.18(\pm 0.05)m_b,$$
$$SD = 0.42, \quad r = 0.85. \quad (5a)$$

If we impose a unit slope, the equation becomes

$$\log_{10}(M_0) = 11.02(\pm 0.28) + 1.00(\pm 0.06)m_b,$$
$$SD = 0.49, \quad r = 0.78, \quad (5b)$$

where the numbers in parentheses are standard errors, SD indicates the standard deviation, and r denotes the correlation coefficient.

5. Discussion and Conclusion

[36] Based on the broadband digital data from regional Lg waves, we obtain a tomographic Q_{Lg} model for Northeast China and its vicinity. The inversions are independently conducted at individual frequencies. There is no a priori constraint on the frequency dependence of the Q model or source spectra applied to the inversion. Limited by the available data, frequency-dependent site responses, source coupling terms, and radiation pattern are not considered in our inversion. At each frequency the Q_{Lg} and the source functions are simultaneously inverted. The simultaneous inversion may introduce trade-offs between the source functions and the Q_{Lg} measurements. For example, at the high-frequency end the trade-off may affect both the high-frequency falloff of the source function and the high-frequency dependence of Q_{Lg}. The conventional Lg group-velocity window of 3.6–3.0 km/s is adopted for calculating the Lg-wave spectra. Given that this window is originally derived for high-frequency observations, additional study should be conducted to check its eligibility for a broad frequency band.

[37] Both Lg-wave amplitudes and noise levels vary within the frequency band, causing different signal-to-noise ratios at different frequencies. The unevenly distributed sources and stations make the ray coverage change geographically. The checkerboard testing method is used to investigate the inversion resolution. The limitation of the checkerboard testing method is that it only qualitatively gives the resolution of the Q distribution. In particular, it does not give any information on the parameter trade-off between the attenuation and source spectral parameters [*Menke et al.*, 2006; *Xie*, 2006]. A full resolution matrix method may solve this problem better [*Phillips et al.*, 2005; *Phillips and Stead*, 2008].

[38] In general, our best data coverage is in Northeast China and between 0.4 and 2.0 Hz, where the Q_{Lg} model has a peak resolution of approximately 1° × 1°. Toward the lower and higher frequencies and in the surrounding region, the resolution deteriorates. The 1 Hz Q_{Lg}, which has the highest spatial resolution, shows an average value of 414 and a
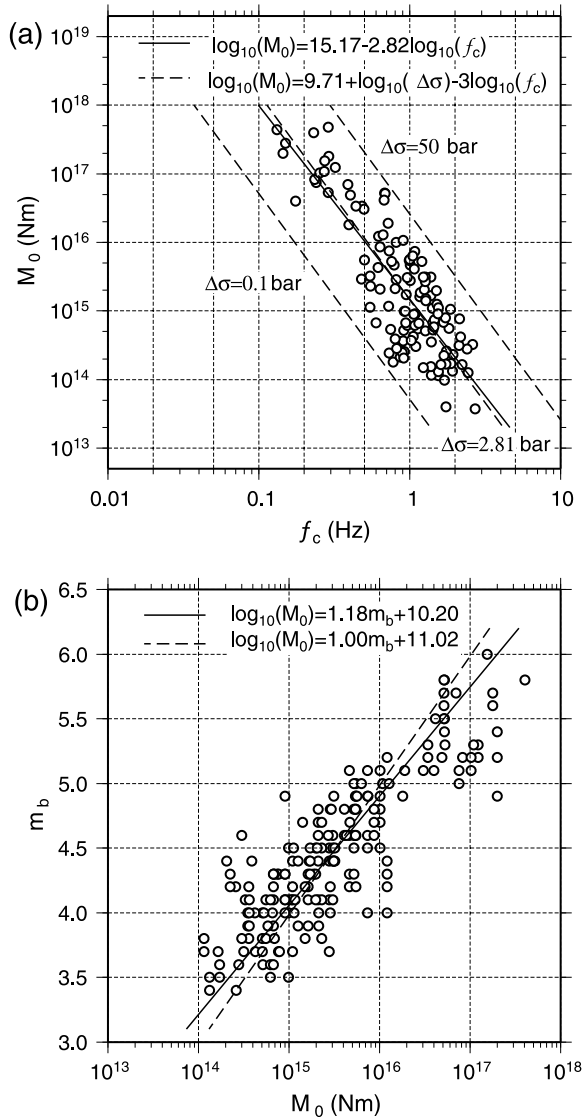
Figure 16. (a) seismic moment M_0 versus corner frequency f_c, where the solid line is the linear regression assuming a constant stress drop, while dashed lines were obtained based on -3 scaling and variable stress drops. (b) Body-wave magnitude m_b versus seismic moment M_0, where the solid line was obtained by linear regression and the dashed line was calculated using a unit slope.

spatial trend of increase from south to north. The model correlates well with local tectonics. The mountain areas, for example, the DMs and CMs, often have higher Q_{Lg} values than the regional mean, whereas the basins are characterized by low Q values. In the overlapped region the current Q_{Lg} model is consistent with previous results [e.g., *Phillips et al.*, 2005; *Pei et al.*, 2006; *Xie et al.*, 2006; *Ford et al.*, 2009], but with an improved resolution and a broader frequency band. The 1 Hz Q_{Lg} model of *Chung et al.* [2007] appears to be systematically higher than our result.

[39] The current Q_{Lg} model is for a relatively broad frequency band. Using a statistical method we investigate the Q_{Lg} frequency dependence both for the entire region and for subregions such as the basins and mountain areas. Within the investigated area the Q_{Lg} values show larger regional variations at lower frequencies (0.2 to 1.0 Hz) than at higher frequencies (above 2.0 Hz). The low-frequency Q_{Lg} appears to have a weak correlation with the crustal thickness. Given that there are multiple factors simultaneously affecting the attenuation, there are still uncertainties in the present inversions. More investigations should be conducted to see if this is an overall feature for Q_{Lg}. However, considering that the scaling parameter for overtone cutoff is *fH*, if a crust 15 km thick can affect the propagation of a 1 Hz *Lg* wave, then it is possible that a crust 30 km thick may affect the propagation of a 0.5 Hz *Lg* wave. At high frequencies the correlation with crustal thickness is not as apparent as at low frequencies (the result is not shown).

[40] The Q_{Lg} has a complex frequency dependence and the commonly adopted power-law Q_{Lg} model may be oversimplified in a broad frequency band, although it may still be a useful approximation within a limited frequency band. The η values, that is, the local slope of the Q_{Lg}-versus-frequency curve, have relatively stable values between 0.5 and 0.8 for large regions. However, for smaller geological units the distribution of η can behave differently; for example, the η values for basins show large scatter due to their complex frequency dependence. The Q_{Lg} is an apparent Q composed of effects from both geometric parameters and physical properties of the crustal waveguide. For example, the strong *Lg*-wave attenuation and its complex frequency dependence in basins can result either from the basin being filled with more absorbing material or because of the change of the waveguide shape. Investigating the frequency dependence of Q_{Lg} adds a new dimension to study of the underlying physics.

[41] Although a priori constraints are not applied, the simultaneously inverted *Lg*-wave excitation spectrum can be reasonably fit into the ω^2 source model [*Street et al.*, 1975; *Sereno at al.*, 1988], which gives the seismic moment M_0 and the corner frequency f_C. A linear relation with a slope of -2.82 is obtained between $\log_{10}(M_0)$ and corner frequency f_C. This slope is close to the theoretical prediction of -3 by *Taylor et al.* [2002]. We also compare the $\log_{10}(M_0)$ with the body-wave magnitudes reported by regional networks. A linear scaling relation with a slope close to unity can be obtained. These relationships are consistent with the previous results and provide additional support for our Q_{Lg} model.

[42] The current Q_{Lg} model, with its refined spatial resolution and improved frequency band, can benefit investigations of regional tectonics. An accurate Q model is vital in characterizing the regional sources including earthquakes and explosions. Northeast China (particularly in these sedimentary basins) is a densely populated area and has frequently experienced major earthquakes (e.g., the M_s 7.3 Haicheng earthquake in 1975 and the M_s 7.8 Tangshan earthquake in 1976). The broadband *Lg*-wave attenuation model also provides a basis for estimation of strong-motion attenuation in this region.

Appendix A: *Lg Q* Inversion

[43] The *Lg*-wave spectral amplitude can be expressed as [e.g., *Xie and Mitchell*, 1990]

$$A(f, \Delta) = S(f)R(f, \theta)G(\Delta)\Gamma(f, \Delta)X(f)r(f), \quad (A1)$$

where f is the frequency, Δ is the epicentral distance, $A(f, \Delta)$ is the *Lg*-wave displacement spectrum, and

$$S(f) = \frac{M_0}{4\pi\rho v_s^3} S'(f) \qquad (A2)$$

is the *Lg*-wave source function, where $S'(f)$ is a normalized source spectrum, M_0 is the seismic moment, and ρ and v_s are the average density and shear wave velocity in the source region.

$$G(\Delta) = (\Delta_0 \Delta)^{-1/2} \qquad (A3)$$

is the geometrical spreading factor, with Δ_0 a reference distance, usually fixed at 100 km [*Street et al.*, 1975; *Hermann and Kijko*, 1983], $R(f,\theta)$ is the source radiation pattern, which can vary with the azimuth θ, and $X(f)$, and $r(f)$ are the frequency-dependent source coupling term and the site response, respectively. Limited by the available data, it is difficult to separate $X(f)$ and $r(f)$ from the source spectrum and the attenuation effects. As a trade-off we neglect these factors by assuming that $X(f) = r(f) = 1$ and their effects will be combined into the source and the attenuation measurements as errors. For the same reason, we neglect the effect of radiation pattern and let $R(f,\theta) = 1$. In equation (A1)

$$\Gamma(f, \Delta) = \exp[-\frac{\pi f}{V} B(f, \Delta)] \qquad (A4)$$

is the attenuation factor, where V is the *Lg*-wave group velocity, and

$$B(f, \Delta) = \int_{ray} \frac{ds}{Q(x,y,f)} \qquad (A5)$$

is the integral of attenuation along the great circle wave path, and $Q(x,y,f)$ is the *Lg*-wave Q, which is a function of the frequency and the surface location (x,y). For attenuation tomography we partition the Q model into rectangular grids and discretize the integral in equation (A5) into a summation,

$$B(f) = \sum_{n=1}^{N} \int_n \frac{ds}{Q(x,y,f)}, \qquad (A6)$$

where n denotes the nth rectangle the ray passes, $\int_n ds$ indicates the integral along the segment in the nth rectangle, and N is the number of segments along the ray.

[44] Applying the natural logarithm to equation (A1), we have

$$\ln[A(f, \Delta)] - \ln[G(\Delta)] = \ln[S(f)] - \frac{\pi f}{V} B(f, \Delta). \qquad (A7)$$

Assuming that the attenuation and source function can be separated into a background part and a perturbation, that is,

$$\frac{1}{Q(x,y,f)} \approx \frac{1}{Q^0(x,y,f)} - \frac{\delta Q(x,y,f)}{[Q^0(x,y,f)]^2}, \qquad (A8)$$

and

$$\ln[S(f)] = \ln[S^0(f)] + \delta\ln[S(f)], \qquad (A9)$$

we have

$$\ln[A(f, \Delta)] - \ln[G(\Delta)] - \ln[S^0(f)] + \frac{\pi f}{V} B^0(f)$$
$$= \delta\ln[S(f)] - \frac{\pi f}{V} \delta B(f), \qquad (A10)$$

where variables with superscript 0 denote their values in the initial model or the transition model from a previous iteration, δQ is the perturbation of the *Lg* Q, $\delta\ln[S(f)]$ is the perturbation of the logarithmic *Lg* source function, and

$$\delta B(f) = \sum_{n=1}^{N} \int_n \frac{\delta Q(x,y,f)}{[Q^0(x,y,f)]^2} ds. \qquad (A11)$$

To calculate the integral in equation (A11) we use the bilinear function

$$Q(x,y) = \sum_{p=1}^{4} a_p w_p(x,y), \qquad (A12)$$

to interpolate Q in each rectangle, where $w_1 = 1$, $w_2 = x$, $w_3 = y$, and $w_4 = xy$. Interpolation coefficients a_P can be obtained from Q values at four corners by solving the fourth-order linear equations using Cramer's rule,

$$a_p = \sum_{l=1}^{4} (-1)^{p+1} \frac{D_{lp}}{D} Q_l, \qquad (A13)$$

where Q_l denotes the Q value at the lth corner, and D_{lp} is the cofactor of the fourth-order determinant D related to the lth corner. From equation (A12) we have

$$\delta Q(x,y) = \sum_{l=1}^{4} \sum_{p=1}^{4} \frac{\partial a_p}{\partial Q_l} w_p \delta Q_l. \qquad (A14)$$

From equation (A13),

$$\frac{\partial a_p}{\partial Q_l} = (-1)^{p+1} \frac{D_{lp}}{D}. \qquad (A15)$$

Substituting equations (A14) into (A11),

$$\delta B(f) = \sum_{n=1}^{N} \sum_{l=1}^{4} \sum_{p=1}^{4} \frac{\partial a_p}{\partial Q_l} \int_n \frac{w_p}{[Q^0(x,y,f)]^2} ds \, \delta Q_l. \qquad (A16)$$

Given that we have multiple sources and stations, then both equation (A10) and equation (A16) can be combined into a linear system,

$$\mathbf{H} = \mathbf{A} \cdot \delta\mathbf{Q} + \mathbf{E} \cdot \delta\mathbf{U}, \qquad (A17)$$

where $\mathbf{H}$ is a vector composed of residuals between the observed and the synthesized *Lg* spectra. Its elements are

$$h_j = \ln[A_j(f, \Delta)] - \ln[G_j(\Delta)] - \ln[S_k^0(f)] + \frac{\pi f}{V} \cdot B_j^0(f), \quad (A18)$$

where j is the index for the rays, and k is the index for sources. Matrix $\mathbf{A}$ is composed of the differential coefficients

that set up the relationship between the Q perturbations and the observed Lg-wave spectra. Its elements are

$$a_{ij} = -\frac{\pi f}{V} \sum_{n=1}^{N_{ij}} \sum_{p=1}^{4} \frac{\partial a_p}{\partial Q_i} \int_n \frac{w_p}{[Q^0(x,y,f)]^2} ds, \qquad (A19)$$

where i is the global index for grid nodes and it has replaced the corner index l in equation (A16), n is the index for ray segments, and N_{ij} is the number of segments in the jth ray that actually involve the Q perturbations at the ith node. $\delta\mathbf{Q}$ is a vector composed of the perturbations of the Q values. Its element δQ_i is the Q perturbation at the ith node. Matrix $\mathbf{E}$ sets up the relationship between the source perturbation and the observed Lg-wave spectra. Its elements e_{kj} are mostly zeros but are equal to 1 when the jth ray is radiating from the kth source. $\delta\mathbf{U}$ is a vector composed of the source perturbations $-\delta\ln[S_k(f)]$.

[45] By minimizing the norm of the residual vector $\mathbf{H}$, we solve the perturbation vectors $\delta\mathbf{Q}$ and $\delta\mathbf{U}$ that are used to update the attenuation model and source functions. Multiple iterations are required owing to the nonlinear relation involved. The LSQR algorithm [*Paige and Saunders*, 1982] with regularization, damping, and smoothing is used to solve the linear equation (A17). It usually converges quickly, and four to six iterations will be sufficient to obtain the result.

References

Al-Damegh, K., E. Sandvol, A. Al-Lazki, and M. Barazangi (2004), Regional seismic wave propagation (*Lg* and Sn) and Pn attenuation in the Arabian Plate and surrounding regions, *Geophys. J. Int.*, *157*, 775–795.

Bouchon, M. (1982), The complete synthesis of seismic crustal phases at regional distances, *J. Geophys. Res.*, *87*, 1,735–1,741.

Brune, J. N. (1970), Tectonic stress and the spectra of seismic shear waves from earthquakes, *J. Geophys. Res.*, *75*, 4997–5009.

Cai, X. L., J. S. Zhu, J. M. Cao, Z. Q. Yan, Z. X. Yang, and X. H. Hong (2002), Structure and dynamics of lithosphere and asthenosphere in the gigantic East Asian-West Pacific rift system (in Chinese with English abstract), *Geol. China*, *29*, 234–245.

Calvert, A., E. Sandvol, D. Seber, M. Barazangi, F. Vidal, G. Alguacil, and N. Jabour (2000), Propagation of regional seismic phases (*Lg* and Sn) and Pn velocity structure along the Africa–Iberia plate boundary zone: tectonic implications, *Geophys. J. Int.*, *142*, 384–408.

Campillo, M. (1987), *Lg* wave propagation in a laterally varying crust and the distribution of the apparent quality factor in central France, *J. Geophys. Res.*, *92*, 12604–12614.

Campillo, M. (1990), Propagation and attenuation characteristics of the crustal phase *Lg*, *Pure Appl. Geophys.*, *132*, 1–20.

Campillo, M., B. M. Feignier, M. Bouchon, and N. Béthoux (1993), Attenuation of crustal waves across the Alpine range, *J. Geophys. Res.*, *98*, 1987–1996.

Chi, G. S. (1988), The study of Cenozoic basalts and upper mantle beneath Eastern China (in Chinese with English abstract), pp. 1–216, China University of Geosciences Press, Wuhan.

Chung, T. W., M.-H. Noh, J.-K. Kim, Y.-K. Park, H.-J. Yoo, and J. M. Lees (2007), A study of the regional variation of low-frequency Q_{Lg}^{-1} around the Korean Peninsula, *Bull. Seismol. Soc. Am.*, *97*, 2190–2197, doi:10.1785/0120070066.

Cong, L., and B. Mitchell (1998), *Lg* coda Q and its relation to the geology and tectonics of the Middle East, *Pure Appl. Geophys.*, *153*, 563–585.

Cong, L., J. Xie, and B. J. Mitchell (1996), Excitation and propagation of *Lg* from earthquakes in central Asia with implications for explosion/earthquake discrimination, *J. Geophys. Res.*, *101*, 27779–27789.

Crosson, R. S. (1976), Crustal modelling of earthquake data, 1. Simultaneous least squares estimation of hypocenter and velocity parameters, *J. Geophys. Res.*, *81*, 3036–3046.

Drouet, S., A. Souriau, and F. Cotton (2005), Attenuation, seismic moment, and site effects for weak-motion events: Application to the Pyrenees, *Bull. Seismol. Soc. Am.*, *95*, 1731–1748, doi:10.1785/0120040105.

Efron, B. (1983), Estimating the error rate of a prediction rule: Improvement on cross-validation, *J. Am. Stat. Assoc.*, *78*, 316–331.

Fan, G. W., and T. Lay (2002), Characteristics of *Lg* attenuation in the Tibetan Plateau, *J. Geophys. Res.*, *107*(B10), 2256, doi:10.1029/2001JB000804.

Fan, G. W., and T. Lay (2003a), Strong *Lg* wave attenuation in the northern and eastern Tibetan Plateau measured by a two-station/two-event stacking method, *Geophys. Res. Lett.*, *30*(10), 1530, doi:10.1029/2002GL016211.

Fan, G. W., and T. Lay (2003b), Strong *Lg* attenuation in Tibetan Plateau, *Bull. Seismol. Soc. Am.*, *93*, 2264–2272.

Feng, Z., C. Jia, X. Xie, S. Zhang, Z. Feng and T. A. Cross (2010), Tectonostratigraphic units and stratigraphic sequences of the nonmarine Songliao basin, northeast China, *Basin Res.*, *22*, 79–95, doi:10.1111/j.1365-2117.2009.00445.x.

Fisk, M. D. (2006), Source spectral modeling of regional P/S discriminants at nuclear test sites in China and the former Soviet Union, *Bull. Seismol. Soc. Am.*, *96*, 2348–2367, doi:10.1785/0120060023.

Ford, S. R., D. S. Dreger, K. Mayeda, W. R. Walter, L. Malagnini, and W. S. Phillips (2008), Regional Aattenuation in Northern California: A comparison of five 1D Q methods, *Bull. Seismol. Soc. Am.*, *98*, 2033–2046, doi:10.1785/0120070218.

Ford, S. R., W. S. Phillips, W. R. Walter, M. E. Pasyanos, K. Mayeda, and D. S. Dreger (2009), Attenuation tomography of the Yellow Sea/Korean Peninsula from coda-source normalized and direct *Lg* amplitudes, *Pure Appl. Geophys.*, doi:10.1007/s00024-009-0023-2.

Gao, X., W. M. Wang, and Z. X. Yao (2005), Crustal structure of China mainland and its adjacent regions (in Chinese), *Chin. J. Geophys.*, *48*, 591–601.

Ge, H., Y. Ni, C. Huang, J. Li, Y. Li, Y. Jiang, and F. Lu (1989), *Lg* velocity, attenuation and magnitude of the continent area in China (in Chinese), *Chin. Sci. Bull.*, *24*, 1889–1892.

Ge, X. H., and W. P. Ma (2007), Mesozoic-Cenozoic tectonic framework of southern Northeast Asia (in Chinese with English abstract), *Geol. China*, *34*, 212–228.

Herrmann, R. B., and A. Kijko (1983), Modeling some empirical *Lg* relations, *Bull. Seismol. Soc. Am.*, *73*, 157–172.

Huang, C., Z. Gao, L. Shi, and Y. Ni (1990), *Lg* wave attenuation and magnitude in Northeast China region (in Chinese), *Northeast. Seismol. Res.*, *6*, 41–49.

Jih, R. S. (1998), Location calibration effects in China, in Proceedings, 20th Annual Seismic Research Symposium on Monitoring a Comprehensive Test Ban Treaty, 21–23 September 1998, pp. 44–45.

Jin, A., and K. Aki (1988), Spatial and temporal correlation between coda Q and seismicity in China, *Bull. Seismol. Soc. Am.*, *78*, 741–769.

Kadinsky-Cade, K., M. Barazangi, J. Oliver, and B. Isacks (1981), Lateral variation in high frequency seismic wave propagation at regional distances across the Turkish-Iranian plateaus, *J Geophys. Res*, *86*, 9377–9396.

Kennett, B. L. N. (1984), Guided wave propagation in laterally varying media; I. Theoretical development, *Geophys. J.*, *79*, 235–255.

Kennett, B. L. N. (1986), *Lg* waves and structural boundaries, *Bull. Seismol. Soc. Am.*, *76*, 1133–1141.

Knopoff, L., F. Schwab, and E. Kausel (1973), Interpretation of *Lg*, *Geophys. J. R. Astron. Soc.*, *33*, 389–404.

Li, X., and X. Yuan (2003), Receiver functions in northeast China—Implications for slab penetration into the lower mantle in Northwest Pacific subduction zone, *Earth Planet. Sci. Lett.*, *216*, 679– 691.

Ma, W. P., S. N. Lu, and G. S. Wang (2003), Tectonic positioning of the islands of Japan in the Mesozoic Asian frontier and its relation to the regional geology of eastern China (in Chinese with English abstract), *Geol. Bull. China*, *22*, 192–199.

Mayeda, K., and W. R. Walter (1996), Moment, energy, stress drop, and source spectra of western United States earthquakes from regional coda envelopes, *J Geophys. Res*, *101*, 11,195–11,208.

McNamara, D. E., T. J. Owens, and W. R. Walter (1996), Propagation characteristics of *Lg* across the Tibetan Plateau, *Bull. Seismol. Soc. Am.*, *86*, 457–469.

Mellors, R., F. Vernon, V. Camp, A. Al-Amri, A. Ghalib, and M. Al-Dail (1999), Regional wave propagation in the Saudi Arabian peninsula, *Geophys. Res. Lett.*, *104*, 20221–20235.

Menke, W., R. C. Holmes, and J. Xie (2006), On the nonuniqueness of the coupled origin time-velocity tomography problem, *Bull. Seismol. Soc. Am.*, *96*, 1131–1139.

Mitchell, B. J., Y. Pan, J. Xie, and L. Cong (1997), *Lg* coda Q variation across Eurasia and its relation to crustal evolution, *J. Geophys. Res.*, *102*, 222767–22780.

Mitchell, B. J., L. Cong, and G. Ekström (2008), A continent-wide map of 1-Hz *Lg* coda Q variation across Eurasia and its relation to lithospheric evolution, *J. Geophys. Res.*, *113*, B04303, doi:10.1029/2007JB005065.

Morgan, J. S., G. L. Christeson, and C. A. Zelt (2002), Testing the resolution of a 3D velocity tomogram across the Chicxulub crater, *Techonophysics*, *355*, 215–226.

Mueller, R. A., and J. R. Murphy (1971), Seismic characteristics of underground nuclear explosions, Part I, Seismic spectrum scaling, *Bull. Seismol. Soc. Am.*, *61*, 1675–1692.

Nuttli, O. W. (1973), Seismic wave attenuation and magnitude relations for eastern North America, *J. Geophys. Res.*, *78*, 876–885.

Nuttli, O. W. (1983), Average seismic source-parameter relations for mid-plate earthquakes, *Bull. Seismol. Soc. Am.*, *73*, 519–535.

Nuttli, O. W. (1986), Yield estimates of Nevada Test Site explosions obtained from seismic *Lg* waves, *J. Geophys. Res.*, *91*, 2137–2151.

Ottemöller, L. (2002), *Lg* wave Q tomography in Central America, *Geophys. J. Int.*, *150*, 295–302.

Ottemöller, L., N. M. Shapiro, S. K. Singh, and J. F. Pacheco (2002), Lateral variation of *Lg* wave propagation in southern Mexico, *J. Geophys. Res.*, *107*(B1), 2008, doi:10.1029/2001JB000206.

Paige, C. C., and M. A. Saunders (1982), LSQR: An algorithm for sparse linear equations and sparse least squares, *ACM Trans. Math. Softw.*, *8*, 43–71.

Patton, H. J., and J. Schlittenhardt (2005), A transportable mb (*Lg*) scale for central Europe and implications for low-magnitude Ms–mb discrimination, *Geophys. J. Int.*, *163*, 126–140.

Pei, S., J. Zhao, C. A. Rowe, S. Wang, T. M. Hearn, Z. Xu, H. Liu, and Y. Sun (2006), M_L amplitude tomography in North China, *Bull. Seismol. Soc. Am.*, *96*, 1560–1566, doi:10.1785/0120060021.

Pei, S., J. Zhao, Y. Sun, Z. Xu, S. Wang, H. Liu, C. A. Rowe, M. N. Toksöz, and X. Gao (2007), Upper mantle seismic velocities and anisotropy in China determined through Pn and Sn tomography, *J. Geophys. Res.*, *112*, B05312, doi:10.1029/2006JB004409.

Phillips, W. S., and R. J. Stead (2008), Attenuation of *Lg* in the western US using the USArray, *Geophys. Res. Lett.*, *35*, L07307, doi:10.1029/2007GL032926.

Phillips, W. S., H. E. Hartse, and S. R. Taylor (2000), 1 Hz *Lg* Q tomography in central Asia, *Geophys. Res. Lett.*, *20*, 3425–3428.

Phillips, W. S., H. E. Hartse, and J. T. Rutledge (2005), Amplitude ratio tomography for regional phases Q, *Geophys. Res. Lett.*, *32*, L21301, doi:10.1029/2005GL023870.

Rao, Y., Y. Wang, and J. V. Morgan (2006), Crosshole seismic waveform tomography: II. Resolution analysis, *Geophys. J. Int.*, *166*, 1237–1248.

Rodgers, A., J. Ni, and T. Hearn (1997), Propagation characteristics of short period Sn and lg in the Middle East, *Bull. Seismol. Soc. Am.*, *87*, 396–413.

Sandvol, E., K. Al-Damegh, A. Calvert, D. Seber, M. Barazangi, R. Mohamad, R. Gok, N. Turkelli, and C. Gurbuz (2001), Tomographic imaging of observed regional wave propagation in the Middle East, *Pure Appl. Geophys.*, *158*, 1121–1163.

Sereno, T. J., Jr., S. R. Bratt, and T. C. Bache (1988), Simultaneous inversion of regional wave spectra for attenuation and seismic moment in Scandinavia, *J. Geophys. Res.*, *93*(B3), 2019–2035.

Shapiro, N., N. Béthous, M. Campillo, and A. Paul (1996), Regional seismic phases across the Ligurian sea: *Lg* blockage and oceanic propagation, *Phys. Earth Planet Inter.*, *93*, 257–268.

Shen, X., H. Zhou, and H. Kawakatsu (2008), Mapping the upper mantle discontinuities beneath China with teleseismic receiver functions, *Earth Planets Space*, *60*, 713–719.

Street, R. L., R. B. Herrmann, and O. W. Nuttli (1975), Spectral characteristics of the *Lg* wave generated by central United States earthquakes, *Geophys. J. R. Astron. Soc*, *41*, 51–63.

Taylor, S. R., A. A. Velasco, H. E. Hartse, W. S. Phillips, W. R. Walter, and A. J. Rodgers (2002), Amplitude corrections for regional seismic discriminants, *Pure Appl. Geophys.* (Special Edition on Monitoring the Comprehensive Nuclear-Test-Ban Treaty: Seismic Event Discrimination and Identification) *159*, 623–650.

Wu, R.-S., and K. Aki (1985), The fractal nature of the inhomogeneities in the lithosphere evidenced from seismic wave scattering, *Pure Appl. Geophys.*, *123*, 805–818.

Wu, R.-S., S. Jin, and X. B. Xie (2000), Energy partition and attenuation of *Lg* waves by numerical simulations using screen propagators, *Phys. Earth Planet Inter.*, *120*, 227–243.

Xie, J. (1993), Simultaneous inversion for source spectrum and path Q using *Lg* with application to three Semipalatinsk explosions, *Bull. Seismol. Soc. Am.*, *83*, 1547–1562.

Xie, J. (2006), Fundamental limitations in resolving power of Q tomography, *Seismol. Res. Lett.*, *77*, 197.

Xie, J., and B. J. Mitchell (1990), Attenuation of multiphase surface waves in the basin and range province: Part I. *Lg* and *Lg* coda, *Geophys. J. Int.*, *102*, 121–137.

Xie, J., and O. W. Nuttli (1988), Interpretation of high frequency coda at large distances: Stochastic modeling and method of inversion, *Geophys. J.*, *95*, 579–595.

Xie, J., R. Gok, J. Ni, and Y. Aoki (2004), Lateral variations of crustal seismic attenuation along the INDEPTH profiles in Tibet from *Lg* Q inversion, *J. Geophys. Res.*, *109*, B10308, doi:10.1029/2004JB002988.

Xie, J., Z. Wu, R. Liu, D. Schaff, Y. Liu, and J. Liang (2006), Tomographic regionalization of crustal *Lg* Q in eastern Eurasia, *Geophys. Res. Lett.*, *33*, L03315, doi:10.1029/2005GL024410.

Xie, M. Q. (2000), Collage plate tectonics and its drive mechanism—The tectonic evolution in Northeast China and its adjacent areas (in Chinese), Science Press, Beijing, pp. 5–11.

Xie, X. B., and T. Lay (1994), The excitation of *Lg* waves by explosions: A finite-difference investigation, *Bull Seismol. Soc. Am.*, *84*, 324–342.

Zelt, C. (1998), Lateral velocity resolution from three-dimensional seismic refraction data, *Geophys. J. Int.*, *135*, 1101–1102.

Zhang, C. K., X. K. Zhang, J. R. Zhao, B. F. Liu, J. S. Zhang, Z. X. Yang, Y. Hai, and G. W. Sun (2002), Study on the crustal and upper mantle structure in the Tianchi volcanic region and its adjacent area of Changbaishan (in Chinese), *Chinese J. Geophys.*, *45*, 813–820.

Zhang, T. R., and T. Lay (1995), Why the *Lg* phase does not traverse oceanic crust, *Bull Seism. Soc. Am.*, *85*, 1,665–1,678.

Zhao, L. F., X. B. Xie, W. M. Wang, and Z. X. Yao (2008), The regional seismic characteristics of the October 9, 2006 North Korean nuclear test, *Bull. Seism. Soc. Am.*, *98*, 2,571–2,589, doi:10.1785/0120080128.

Zor, E., E. Sandvol, J. Xie, N. Türkelli, B. Mitchell, A. H. Gasanov, and G. Yetirmshli (2007), Crustal attenuation within the Turkish Plateau and surrounding regions, *Bull. Seism. Soc. Am.*, *97*, 151–161, doi:10.1785/0120050227.

W.-M. Wang, Institute of Tibetan Plateau Research, Chinese Academy of Sciences, Beijing 100864, China.

X.-B. Xie (correspondence author), IGPP/CSIDE, University of California, Santa Cruz, 1156 High Street, Santa Cruz, CA 95064, USA. (xie@pmc.ucsc.edu)

Z.-X. Yao, J.-H. Zhang, and L.-F. Zhao, Institute of Geology and Geophysics, Chinese Academy of Sciences, Beijing 100864, China. (zhaolf@mail.igcas.ac.cn)